

AMERICAN UNIVERSITY OF BEIRUT

3D THERMO-MECHANICAL FINITE ELEMENT
MODELING OF FRICTION STIR WELDING OF SIMILAR
AND DISSIMILAR METALLIC JOINTS WITH COOLING

by
ALI HACHEM KHEIREDDINE

A thesis
submitted in partial fulfillment of the requirements
for the degree of Master of Engineering in Mechanical Engineering
to the Department of Mechanical Engineering
of the Faculty of Engineering and Architecture
at the American University of Beirut

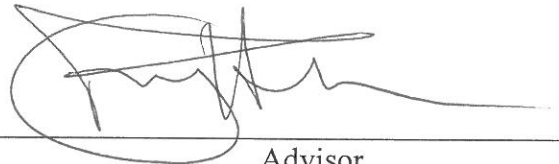
Beirut, Lebanon
April 2013

AMERICAN UNIVERSITY OF BEIRUT

3D THERMO-MECHANICAL FINITE ELEMENT
MODELING OF FRICTION STIR WELDING OF SIMILAR
AND DISSIMILAR METALLIC JOINTS WITH COOLING

by
ALI HACHEM KHEIREDDINE

Approved by:



Dr. Ramsey Hamade, Professor
Department of Mechanical Engineering

Advisor

Dr. Mutasem Shehadeh, Assistant Professor
Department of Mechanical Engineering



Member of Committee

Dr. Elie Hantouche, Assistant Professor
Department of Civil Engineering


Member of Committee

Date of thesis/dissertation defense: 4 April, 2013

AMERICAN UNIVERSITY OF BEIRUT

THESIS RELEASE FORM

I, Ali Hachem Kheireddine

authorize the American University of Beirut to supply copies of my thesis to libraries or individuals upon request.

do not authorize the American University of Beirut to supply copies of my thesis to libraries or individuals for a period of two years starting with the date of the thesis deposit.

Signature

Date

ACKNOWLEDGEMENTS

First of all, I would like to thank my advisor Professor R.F. Hamade for his continuous support, guidance and inspiration throughout my graduate studies. I am also grateful to him for providing me with excellent research facilities and enormous opportunities to attend various international conferences. I would like to thank Prof. M.A. Shehadeh for his constructive feedback during my research. I would like to thank my friend A. H. Ammouri for his valuable insights and suggestions that helped me overcome various impediments I encountered at different stages of research. Special thanks goes to all the group members of the Process, Simulation, and Materials Modeling Research Group ((ProSiMM-RG) at AUB for their support and encouragement throughout my research. I would also like to thank my family and friends who helped me accomplish this work.

Above all, I am very grateful to Great God for His endless graciousness and guidance throughout all of my academic studies.

AN ABSTRACT OF THE THESIS OF

Ali Hachem Kheireddine for Master of Engineering
Major: Mechanical Engineering

Title: 3d Thermo-Mechanical Finite Element Modeling Of Friction Stir Welding Of Similar And Dissimilar Metallic Joints With Cooling

Friction stir welding (FSW), a solid-state metal joining technique, was introduced in 1991 and since then it has become the standard method of welding in many applications. The resulting weld's microstructure and thus weld quality and strength varies greatly depending on input process variables such as tool feed and speed, tilt angle, and tool geometry. Therefore, it is imperative that accurate modeling of this complex process is available to provide proper guidance for selecting the suitable combination of input parameters. Researchers have succeeded in thermo-mechanically modeling of FSW similar aluminum joints but none of the developed models fully simulated the FSW of magnesium, steel or dissimilar aluminum -magnesium joints. This work presents the results of four thermo-mechanical finite element simulations (utilizing a commercial FEM software, DEFORM) for friction stir welded similar and dissimilar metallic joints. Using proper material's flow stress constitutive equations, four FE models were developed for: (1) similar aluminum joints, (2) similar magnesium joints, (3) similar mild carbon steel joints, and (4) dissimilar aluminum-magnesium joints. Once the boundary and contact conditions of the models and were systematically calibrated, it was possible to numerically determine the relevant state variables of interest (strains, strain rates, temperatures, and microstructural phase transformations). These results and other results related to the material flow were successfully validated against experimental results found in the literature for all four cases. Also, determined from the numerical simulations were estimates of the resulting grain size at the weld. For example, it was found that in-process cooling during FSW of similar magnesium and aluminum joints would result in the decrease of grain size. However, decreasing the cooling rate during FSW of carbon steels would decrease the formation of brittle martensite in the weld center.

Keywords: Friction Stir Welding, Finite Element Modeling, dissimilar joints

CONTENTS

I. INTRODUCTION	1
A. FSW Background.....	1
1. <i>Process</i>	1
2. <i>Advantages</i>	3
3. <i>Applications</i>	5
B. FSW Experimental Review	6
1. <i>Similar Joints</i>	6
2. <i>Dissimilar Joints</i>	8
C. FSW Simulation Review	9
1. <i>Similar Joints</i>	10
2. <i>Dissimilar Joints</i>	11
II. THESIS CONTRIBUTION AND APPROACH.....	12
III. FEM FSW MODELS	14
A. Aluminum Similar Model.....	14
1. <i>Parts and Meshes</i>	14
2. <i>Material Modeling</i>	16
3. <i>Friction Modeling</i>	18
4. <i>Boundary Conditions</i>	18
5. <i>Cooling Simulation</i>	20
6. <i>Grain Size Prediction</i>	21
B. Magnesium Similar model.....	23
1. <i>Parts and Meshes</i>	23
2. <i>Material Modeling</i>	25
3. <i>Friction Modeling</i>	25
4. <i>Boundary Conditions</i>	27
5. <i>Grain Size Prediction</i>	29
C. Steel Model	29
1. <i>Parts & Meshes</i>	29
2. <i>Material Modeling</i>	31
3. <i>Friction Modeling</i>	34

4. <i>Boundary Conditions</i>	35
D. Aluminum Magnesium Dissimilar Model	36
1. <i>Parts and Meshes</i>	36
2. <i>Material Modeling</i>	38
3. <i>Friction Modeling</i>	40
4. <i>Separation Criterion</i>	40
5. <i>Boundary Conditions</i>	41
IV. MODEL VALIDATION AND RESULTS	42
A. Aluminum Similar Model	42
1. <i>Model Validation</i>	42
2. <i>Stress Distribution</i>	47
3. <i>Effect of Cooling</i>	47
B. Magnesium Similar Model	49
1. <i>Model Validation</i>	49
2. <i>Temperature Profile</i>	51
3. <i>Effect of the Spindle Speed</i>	53
4. <i>Effect of Cooling Rate</i>	57
C. Steel Model	58
1. <i>Model Validation</i>	58
2. <i>Effect of advancing speed on temperature</i>	61
3. <i>Strain Distribution</i>	61
4. <i>Phases Transformation</i>	62
5. <i>Effect of In-process Laser Heating</i>	67
D. Aluminum Magnesium Dissimilar Model	68
1. <i>Model Validation</i>	68
2. <i>Temperature Contours</i>	74
3. <i>Material flow</i>	76
4. <i>Strain Profile</i>	77
5. <i>Strain rate Profile</i>	78
V. CONCLUSIONS	80
VI. FUTURE WORK	82

VII. RELEVANT PUBLICATIONS	83
A. Refereed Papers	83
VIII. REFERENCES	85

ILLUSTRATIONS

Figure	Page
1: The stages of FSW: (a) Plunge stage, (b) Traverse stage, (c) Retreat stage.....	2
2: Illustration of FSW	3
3: The mesh of the tool, backing plate, and workpiece of the aluminum FEM model...	15
4: The mesh showing nodes with fixed boundary condition (colored in red)	19
5: The workpiece surfaces defined with convection heat transfer.....	19
6: Conduction heat transfer condition at tool-workpiece interface (green nodes) and at the backing plate-workpiece interface (blue nodes).	20
7: The meshed magnesium FEM model	24
8: Friction coefficient vs. temperature as used in FE model; shown compared with experimental data [73]	26
9: The meshed FE model showing the tool, workpiece, and backing plate (under the workpiece). Shown superimposed is a rendering of the in-process laser source.....	31
10: The iron-iron carbide phase diagram [78]	33
11: Isothermal transformation diagram of iron-carbon alloy of eutectoid composition [78].....	33
12: Continuous cooling transformation diagram of eutectoid iron-carbon alloy [78]....	34
13: The mesh of the tool, backing plate, and workpiece for the Al/Mg Model.....	38
14: The volume fractions of elements at initial step.....	39
15: Temperature history of a node 8mm away from the weld line for a period of 3.5 seconds.....	43
16: Temperature Contour in the workpiece	43

17: Temperature distribution for a section parallel to the weld line on the advancing side of the pin as the tool commences.....	45
18: Grain size distribution across the weld line.....	46
19: Effective stress distribution around welding area right after the dwelling phase.....	46
20: Distribution of the grain size across the weld line for: no cooling, back plate cooling, and CO2 cooling.....	48
21: Distribution of $\ln(Z)$ across the weld line for: no cooling, back plate cooling, and CO2 cooling.....	48
22: Experimental vs. simulated temperature profiles for the case 1 described in Table 7.....	50
23: Experimental vs. Simulated temperature profiles for the case 2 described in Table 7.....	51
24: Temperature distribution along the weld section in the Mg model.....	52
25: Variation of strain rate as function of tool rotational speed compared with results from equation 9.....	55
26: Variation of the maximum temperature of the observation point as function of tool rotational speed.....	55
27: Variation of the average grain size as function of the tool rotational speed obtained from the FE model.....	56
28: Variation of the maximum average grain size with the tool rotational speed for different cooling conditions.....	57
29: Temperature contour plot in workpiece for case 2.....	59
30: Simulation Temperature Profile with experimental [24] peak temperature for case 1.....	60

31: Peak temperatures versus advancing speed for experimental [24] and simulation test cases	61
32: Effective strain distribution across the weld section for both test cases.....	62
33:Phase transformation with time as the tool moves away for the normal friction stir welding (RPM=600; V=400 mm/min)	64
34: Phase transformation with time as tool moves away for laser assisted friction stir welding (RPM=600; V=400 mm/min)	65
35: Continuous Cooling Transformation Diagram with FSW model cases superimposed	66
36: SEM image of the stir zone for transverse speed = 400 [24].....	67
37: FEM point tracking snapshots from initial position (left) to final (right) for a particle placed in the magnesium plate.....	69
38: Steel shot initial and final positions [52]	69
39: A comparison between the experimental macrograph (a) [51] and FEM weld section (b).....	70
40: Al-Mg phase diagram (a) and crystallographic data (b) [84]	71
41: SEM image showing the microstructure of the Al/Mg interphase [51].....	71
42: Temperature history for a point placed 6mm from the weld line in the aluminum advancing side.....	73
43: Temperature history for a point placed 6mm from the weld line in the magnesium retreating side.....	73
44: Workpiece Top surface temperature contours by time (a) to (h).....	75
45: Top view Snapshots (b) before mixing (a) after mixing.....	76

46: Sections before and after the pin during welding with locations shown in Figure 45	77
47: Effective stain (mm/mm) at the weld section right behind the pin of the tool	78
48: Effective strain rate during DFSW model (a) general profile (b) weld section.....	79

TABLES

Table	Page
1: Key benefits of friction stir welding [1]	4
2: Various applications of Friction Stir Welding [2]	5
3: Mechanical and thermal properties of AL7075-T6	17
4: AL7075 material constants used for Z (from [68])	22
5: Material properties of AZ31b used in the model.....	25
6: Phase Transformation Models	32
7: Al and Mg material properties and constants summary	39
8: Processing parameters of the validation test cases	49
9: Test cases at a traverse speed of 90 mm/min.....	53
10: Processing parameters of the validation test cases for steel model	58

CHAPTER I

INTRODUCTION

A. FSW Background

Friction stir welding (FSW) is a solid state joining process invented at the Welding Institute, TWI, in Cambridge, UK in 1991. FSW involves a rotating pin tool plunged between the workpieces then advanced along the weld line as illustrated in Figure 1. Due to friction between tool and work, heat is generated causing extensive plastic deformation (hot and heavily plasticized, work does not melt). The tool rotation forces the softened material to flow from the front of the tool towards the back causing the two parts to join.

1. Process

The FSW process can be divided into three stages as shown in Figure 1: the plunge stage, the transverse stage and the retreat stage. In the plunge stage, the tool is plunged between the pieces to be welded at a low speed. If the temperature required for welding is not reached, some may add a dwelling phase before the transverse in order to achieve the required temperature. After that, comes the transverse phase in which the tool moves linearly across the welding line. At the end, comes the retreat stage where the tool is removed from the joint.

The two parts to be welded are usually classified as either advancing side or retreating side as shown in Figure 2. In the advancing side the material are being rotated

in the same direction of the traverse movement of the tool. While in the retreating side are being rotated in the opposing direction of that of the traverse movement of the tool.

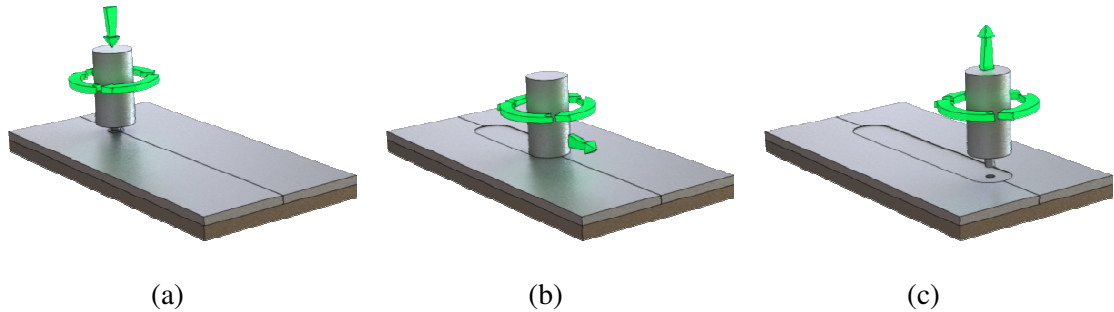


Figure 1: The stages of FSW: (a) Plunge stage, (b) Traverse stage, (c) Retreat stage

More specifically, the welding area shown in Figure 2 can be divided into three main zones: stir zone (SZ), thermo-mechanically affected zone (TMAZ), and heat-affected zone (HAZ). Starting with the stir zone, it is the zone where most severe mechanical deformation heating caused by friction takes place. In this zone, continuous dynamic recrystallization (CDRX) is believed to occur in which new fine grains are recrystallized developing a new weld microstructure. The thermo-mechanically affected zone (TMAZ) is the area surrounding the stir zone. This area is subject to both mechanical deformation and thermal effects but CDRX does not occur in this zone due to the relatively lower deformation strains [1]. The heat-affected zone (HAZ) is the area subject to thermal effects only without any mechanical deformations. The rest material is unaffected bulk material.

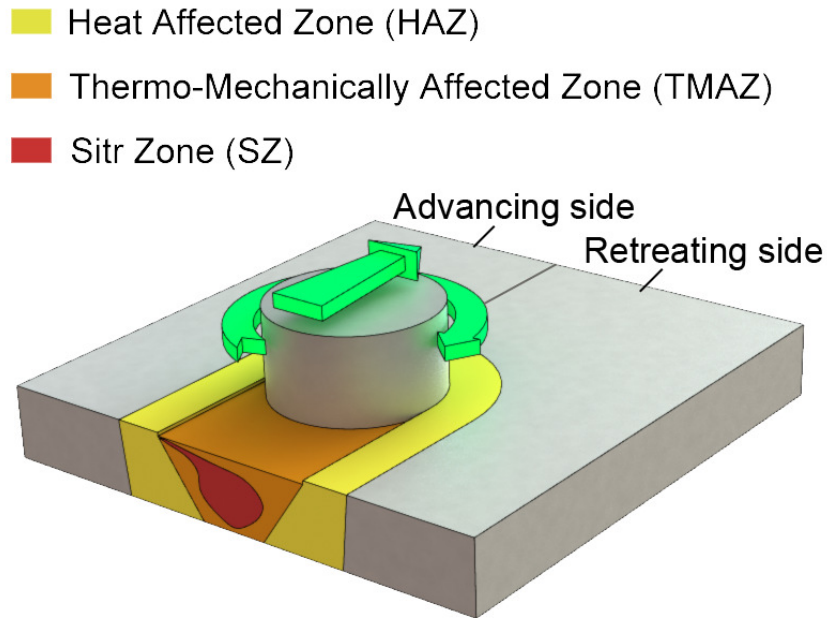


Figure 2: Illustration of FSW

FSW includes many input (processing) parameters that affect directly the microstructural properties and thus the mechanical properties of the weld. Therefore, must be properly selected before welding commences. Some of these parameters are: tool Rotational speed, tool feed, plunge depth, tool geometry, cooling conditions.

2. Advantages

FSW has become an indispensable joining technique with many advantages claimed by FSW. Some of these advantages are listed in Table 1. These advantages lead to the utilization of FSW in many applications replacing traditional welding techniques.

Table 1: Key benefits of friction stir welding [1]

Metallurgical benefits	Environmental benefits	Energy benefits
<ul style="list-style-type: none"> • Solid phase process • Low distortion of workpiece • Good dimensional stability and repeatability • No loss of alloying elements • Excellent metallurgical properties in the joint area • Fine microstructure • Absence of cracking • Replace multiple parts joined by fasteners 	<ul style="list-style-type: none"> • No filler wire required • No arc, fumes or spatter • No shielding gas required • No surface cleaning required • Eliminate grinding wastes • Eliminate solvents required for degreasing • Consumable materials saving such as rags, wire or any other gases 	<ul style="list-style-type: none"> • Only 2.5% of the energy needed for a laser weld • Decreased fuel consumption in light weight aircraft, automotive and ship applications

3. Applications

Since its invention, FSW invaded many civilian and military industries replacing traditional welding techniques. Till the moment, many FSW applications are being introduced. Table 2 shows some applications of FSW divided by sector [2].

Table 2: Various applications of Friction Stir Welding [2]

Shipbuilding and Marine Construction	Aerospace Industry	Railway Industry	Automotive
<ul style="list-style-type: none"> • Panels for decks, sides, bulkheads and floors • Hulls and superstructures • Helicopter landing platforms • Marine and transport structures • Masts and booms, e.g. for sailing boats • Refrigeration plant 	<ul style="list-style-type: none"> • Wings, fuselages, empennages • Cryogenic fuel tanks for space vehicles • Aviation fuel tanks • External throw away tanks for military aircraft • Military and scientific rockets • Repair of faulty MIG welds 	<ul style="list-style-type: none"> • High speed trains • Rolling stock of railways, underground carriages, trams • Railway tankers and goods wagons • Container bodies 	<ul style="list-style-type: none"> • Engine and chassis cradles • Wheel rims • Attachments to hydro-formed tubes • Space frames, e.g. welding extruded tubes to cast nodes • Truck bodies & tail lifts for lorries • Mobile cranes • Armor plate vehicles • Fuel tankers • Caravans • Buses and airfield transportation vehicles

B. FSW Experimental Review

In most of the cases, numerical modeling follows successful experimental trials for optimization purposes. Therefore, in this section a brief review on the experimental FSW will be discussed. The joints reviewed will cover both similar and dissimilar joints. The materials involved in this review are mainly aluminum, magnesium and steel alloys. However, in literature different materials were welded using FSW starting from lightweight such as copper [3-7] or titanium [8-13] reaching heavy metals such as steels [14-24].

1. Similar Joints

For steel and other high-temperature materials, the application of FSW is limited to the presence of suitable tools that can operate in the temperature range of 1000 to 1200 °C [20]. This is due to the fact that the heat produced by stirring and friction is not sufficient to soften the material around the rotating tool. Therefore, it is important to select tool materials with good wear resistance and toughness at temperatures of 1000°C or higher [21]. However, in the past five years, studies have reported that FSW achieves similar grain improvements in the stir zone of steels similar to the ones observed for aluminum. The microstructure and mechanical properties of carbon steel joints are significantly affected by the following factors: heat input during welding, the composition of steel metal used and the processing history of the welded base material [22]. FSW has a significant role in the refinement of ferrite and austenite phases through dynamic recrystallization. In turn, the small sized grains obtained increase the hardness and strength of the stir zone. As a result, weld transverse tensile failures consistently occur near the border of the stir zone which exhibits almost the

same yield and ultimate tensile strengths as the base material [23]. For high carbon steels, strong joints consisting of a refined two-phase structure ferrite and pearlite can be formed through adding heat sources which prevents martensite formation. The low heat inputs in FSW are expected to minimize the distortion and the residual stresses in steels enhancing the ability to weld thick components together. This adds to the ability of FSW to eliminate the weld fumes and the problems caused by hydrogen cracking in steels due to the solid-state nature of FSW process [1]. Sun et. al studied the effect of laser preheating on the welding parameters, final microstructure and mechanical properties of the joints in S45C steel. The experimental results shows how heating helps in increasing the welding speed along with maintaining mechanical properties S45C steel FSWed joints [24].

Similar aluminum alloys are the most successful friction stir welded joints. FSW is used widely in these joints because of the difficulty and disadvantages faced in traditional welding of aluminum causing defects such as crack and porosity [25]. Some of the aluminum alloys welded using FSW are: Al2017 [25], 2014-T651 [26], 2024-T3 [27], 2024-T6 [28,29], 2195-T8 [30,31], 6061-T5 [32,33], Al6063 [34], 6082-T5 [35], 7075-T651 [36] and 7475-T76 [37].

Magnesium alloys are light-weight alloys used in many aerospace and automotive applications mainly because of their high specific strength and stiffness. However, the traditional fusion welding of magnesium produces some defects such as porosity and hot crack weakening their mechanical properties [38]. On the other hand,

using FSW in magnesium welding proved to enhance the mechanical properties of the weld relative to fusion welding. Many publications investigated the FSW of magnesium; some of the alloys studied are: AZ31 [39-40], AZ61 [41], AZ91 [42-45], AM50 [46] and AM60 [46-47].

2. **Dissimilar Joints**

Dissimilar friction stir welding (DFSW) is an interesting variation of FSW where two different metals are joined. The generation of different phases due to phase transformation between different metals only adds to the complexity of trying to simulate DFSW. Of the many successful welding experiments reported in the literature, this review is concerned only with aluminum-magnesium FSW joints. In [48], the authors successfully welded of Al alloy 1050 and Mg alloy AZ31 using FSW. It was concluded that an intermetallic compound $Al_{12}Mg_{17}$ was formed at the weld center with significant higher hardness. In [49], Somasekharan studied the microstructure of an FSW weld formed between AZ91D and AL 6061-T6. Dynamic recrystallization was observed at the weld region causing a decrease in grain size and higher hardness [49]. FSW weld was formed between AZ31 and Al 5052 and grain refinement was found to take place at the stir zone along with hardness increase [50]. Moreover, cooling in dissimilar FSW was demonstrated to enhance the properties of the weld. For example, in [51] underwater FSW was compared to air FSW of Al5083 and Mg AZ31. It was concluded that under water FSW caused a decrease in the peak temperature thus limiting the formation of the intermetallic compound and which resulted in smoother interface compared to air FSW.

It was concluded in [52] that to reach a defect-free weld line between Al/Mg, the harder metal must be placed in the advancing side and the tool should be offset to the same harder metal. It was also found that heat treatment of welded specimens could directly affect the mechanical properties. In [53], the effect of tool configuration and welding parameters on mechanical and microstructural properties in the FSW of AA5754/AZ31 were investigated. It was determined that placing of aluminum in the advancing side and using a pinned tool rather than a “pin-less” tool lead to a better surface appearance and better mechanical properties. The effect of tool shoulder diameter to plate thickness ratio on tensile properties of AA6061 and AZ31B was studied in [54] with a ratio of 3.5 leading to enhanced tensile properties of welds.

C. FSW Simulation Review

With traditional experiments believed to be time and money consuming, significant efforts are increasingly being spent on optimizing and enhancing FSW via numerical simulations. Although researches for years have successfully simulated many aspects of FSW, but due to the large deformation taking place it is still a complex process to simulate. Early on, models of the friction stir processes used thermal models to simulate the heat generation in the process separately from mechanical stress and strain calculations. Later, more accurate models incorporated finite elements capable of handling coupled thermo-mechanical analyses with several commercial software such as DEFORM and ABAQUS.

1. **Similar Joints**

Reports of numerical simulations in the literature appear to utilize models based either on computational fluid dynamics (CFD) methods or solid mechanics methods. Although CFD –based simulations (e.g., [55]) modeled features of the material flow in the process but often led to overestimations of load predictions and /or inaccurate temperature profiles. On the other hand, Schmidt and Hattel [56] used ABAQUS with arbitrary Lagrange–Eulerian (ALE) formulation for performing the dynamic, coupled thermo-mechanical analysis of the FSW process. Buffa [57] developed a 3D Lagrangian implicit, coupled, rigid-viscoplastic, thermo-mechanical model using DEFORM 3D which was able to predict temperature, strain profiles, material flow and their results were validated against experimental results. More recently, Butan and Monaghan [58] performed FSW simulations using DEFORM which showed good agreement with experimental results but an initial high temperature was assigned to the work and their 3D model simulated only the retreating side of the weld. Buffa et al. [57], and through utilizing the principle of continuous dynamic recrystallization (CDRX) and the Zener-Hollomon parameter (Z parameter) were able to determine the average grain size in generated friction stir welds. Richards et al. [60] applied CO₂ cryogenic cooling to FSW and used FEM analysis along with experimental validations to model residual stresses. The authors modeled the tool as a heat source where no mechanical deformations took place. The results suggested that process cooling can help control residual stresses that occur in FSW. [60]

2. Dissimilar Joints

The promising successful results in DFSW along with very accurate results in numerical FSW are good incentives to simulate DFSW. Very poor work in literature focuses on numerically simulating dissimilar FSW.

Using ABAQUS [61], Jamshidi et al. presented a thermo-mechanical behavior and microstructural events in dissimilar friction stir welding of AA6061-T6 and AA5086-O. It was found that placing the AA5086 in the advancing side leads to a more efficient mixing in the weld nugget resulting in a larger thermally affected region. Moreover, it was found that equiaxed fine grains were produced in AA6061 side compared to AA5086 side. In [62], a 3D finite element model was built in ANSYS to study the thermo-mechanical history of the Al/Cu bimetallic lap joints where the tool was modeled as a heat source to avoid modeling difficulties. Using ABAQUS in [63], functionally graded materials (FGM) were utilized to develop a model for Al/Fe dissimilar FSW joint. Only thermal stresses were taken into account and results were in fair agreement with experiments. In [64], Li et al. developed 3D FEM code for Al/Fe FSW joints also using the FGM concept. The tool was modeled as a heat input source and thermal stress and strains were investigated. Li et al. also [65] built a 3D FEM model for aluminum and steel dissimilar FSW using FGM in ABAQUS. Moreover, the FGM used was time varying where the volume of the nugget zone increases with time. Thermal results were compared to experimental data and good agreements were reached.

CHAPTER II

Thesis Contribution and Approach

From all the previous literature we can conclude that basically there are enough experimental results for similar and dissimilar Al/Mg joints for the later FEM to be validated with. Concerning FEM modeling, the most common and successful models are for similar Al joints, and then comes similar Mg joints, and very few are on steel or dissimilar Al/Mg joints (none are fully 3D thermo-mechanically coupled model). Concerning the FE software, DEFORM commercial software (Scientific Forming Technologies Corporation, 2545 Farmers Drive, Suite 200, Columbus, Ohio 43235) was chosen due to its enormous capabilities in accounting for all thermal and mechanical deformations [66]. Moreover, DEFORM has advanced microstructural analysis and phase transformation capabilities which are rarely found in any FE software and will be used in this work.

Accordingly, the four main objectives of this thesis are:

- 1) Develop a 3D Aluminum-Aluminum thermo-mechanical FSW model similar to models found in literature and validate the model with experimental data published. Add cooling to study its effect on the microstructure of the weld.
- 2) Develop a 3D Magnesium-Magnesium thermo-mechanical FSW model and validate the model with experimental data published. Add cooling to study its effect on the microstructure on the weld. Alter processing parameters to study their effect on the weld microstructure.

- 3) Develop a 3D Carbon Steel thermo-mechanical FSW model and validate the model with experimental data published. The model should account for phase transformations taking place which affect the final microstructure. Add laser heating and study its effect on the final micro-constituents of the weld.
- 4) Develop a 3D dissimilar Aluminum-Magnesium thermo-mechanical dissimilar FSW model and validate the model with experimental data published. The model must be able to capture the mixing at the interface between Mg and Al.

CHAPTER III

FEM FSW MODELS

D. Aluminum Similar Model

1. Parts and Meshes

The model geometry consists of 3 parts: tool, workpiece, and backing plate. The tool is a 3 mm diameter pin (2.8 mm long) and a 10 mm diameter shoulder. The pin is considered to be smooth and un-threaded and the tool was tilted 2 degrees about the vertical axis. The workpiece is 90 mm x 60 mm² with height of 3 mm. The backing plate has the same dimensions as the workpiece. These entities are shown (meshed) in Figure 3. While the tool and backing plate were modeled as rigid undeformable bodies, the workpiece was modeled as a plastic body. Since modeling the workpiece as 2 separate bodies at the welding line would create contact instabilities, the weld line assumed to be originally mended.

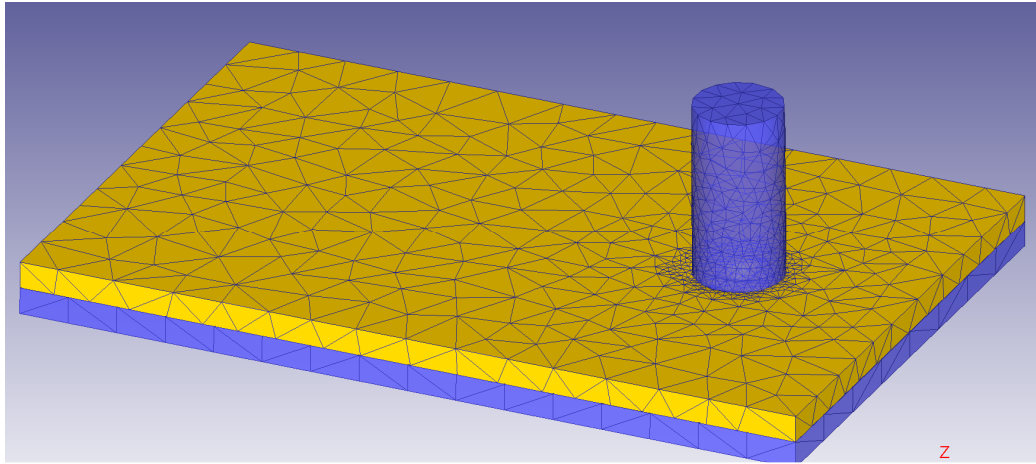


Figure 3: The mesh of the tool, backing plate, and workpiece of the aluminum FEM model

In the first (approach) phase of welding, the tool was set to rotate at 1000 RPM while plunging at a speed of 0.1 mm/s until the shoulder sinks in the workpiece with a depth of 0.1mm. In the second (dwell) phase, the tool was set to dwell for 0.5 sec before the third (traverse) phase commenced where linear motion was set with a speed of 2.5 mm/s.

In any FEM simulation, the two main factors, element size and time step, directly affect the simulation run time and the result's conversion. Here, we address these factors as treated in this work. A mesh made up of tetrahedral element was used in the FEM model with active re-meshing triggered by a relative interference ratio of 0.7 between contacting edges (to ensure the integrity of the workpiece geometry during deformation). Since adaptive meshing was adopted, the actual number of elements would vary through the analyses. However, the tool and the backing plate components were meshed (for heat dissipation only) with each component containing initially

around 5000 elements. The initial number of elements of workpiece was about 10000 elements.

To further capture the state variables at the tool-workpiece interface, a cylindrical mesh control window was applied around the area of interest where fine mesh with elements of size 0.75 mm were created.

2. Material Modeling

The material used for the tool and backing plate was steel AISI 1075. The work material is Aluminum AL7075-T6 which was modeled as a rigid visco-plastic material according to the constitutive equation

$$\sigma = KT^A \dot{\bar{\epsilon}}^B \bar{\epsilon}^C \quad (1)$$

Where flow stress depends on the temperature, strain rate, and strain and where $K=2.69e10$, $A=-3.3155$, $B=0.1324$, and $C=0.0192$ [57]. Other mechanical and thermal characteristics of AL7075-T6 are listed in Table 3.

Table 3: Mechanical and thermal properties of AL7075-T6

Property	Value
Young's Modulus	68900 MPa
Thermal conductivity	180 N/(s K)
Heat capacity	2.433 N/(mm ² °C)
Emissivity	0.7

To account for the continuous dynamic recrystallization (CDRX) occurring in the FSW process, an analytical model for the grain size evolution was implemented. The average grain size is dependent on the strain, strain rate and temperature according to

$$D_{CDRX} = C_1 \varepsilon^k \dot{\varepsilon}^j D_0^h e^{\left(\frac{Q}{RT}\right)} \quad (2)$$

The constants in the Equation 2 were taken from experimental data reported by Buffa et al. [57] leading to

$$D_{CDRX} = 100 \varepsilon^{-0.1648} \dot{\varepsilon}^{-0.322} D_0^{-0.104} e^{\left(\frac{Q}{RT}\right)} \quad (3)$$

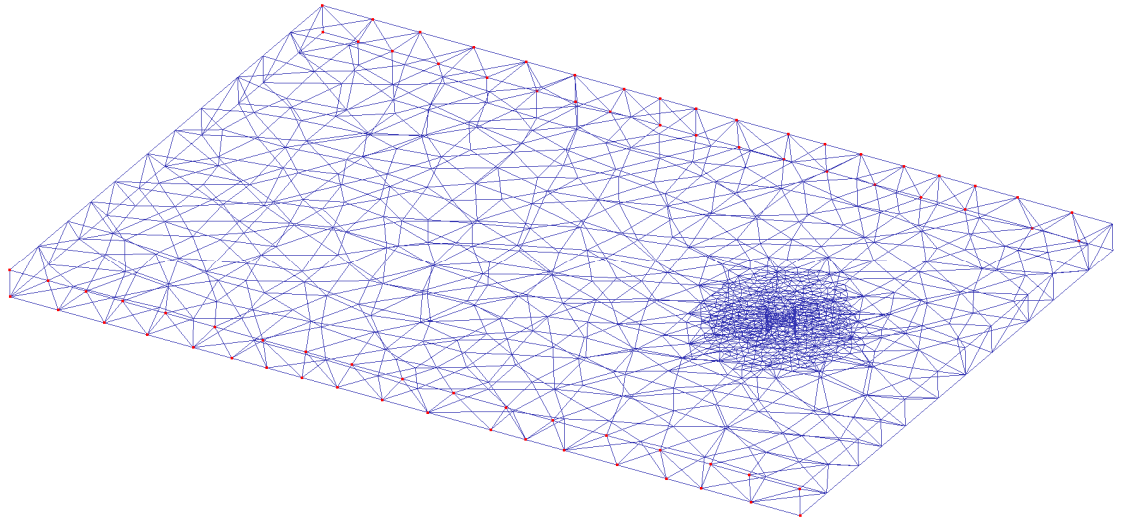
3. **Friction Modeling**

A constant shear friction factor of 0.46 was used at the contact interface between the tool and the workpiece as suggested by Buffa et al. [57].

4. **Boundary Conditions**

The workpiece was fixed from the two sides by setting the velocity of the relevant surface nodes to zero in three directions as shown in Figure 4. For all surface elements facing the surrounding environment, heat convection was accounted for by using a convective heat coefficient of $20 \text{ W}/(\text{m}^2 \text{ }^\circ\text{C})$ at a constant temperature of $25 \text{ }^\circ\text{C}$. Elements with convection heat transfer are shown in Figure 5. The conduction heat transfer coefficient between the tool-workpiece and backing plate-workpiece interfaces was set to $11 \text{ N}/(\text{mm s } ^\circ\text{C})$ [57] as shown in Figure 6.

Selecting the time step is very crucial since setting the time step to very small values would lead to extremely long calculation times while setting it to very large values would result in rapid mesh distortion and/or convergence problems and generally to unreliable output. To get accurate simulations the time step should be selected such that the rotating tool peripheral speed would travel across the minimum element length (0.75 mm) over at least 4 steps. Doing the math yields a time step of 0.0002 s.



5.

Figure 4: The mesh showing nodes with fixed boundary condition (colored in red)

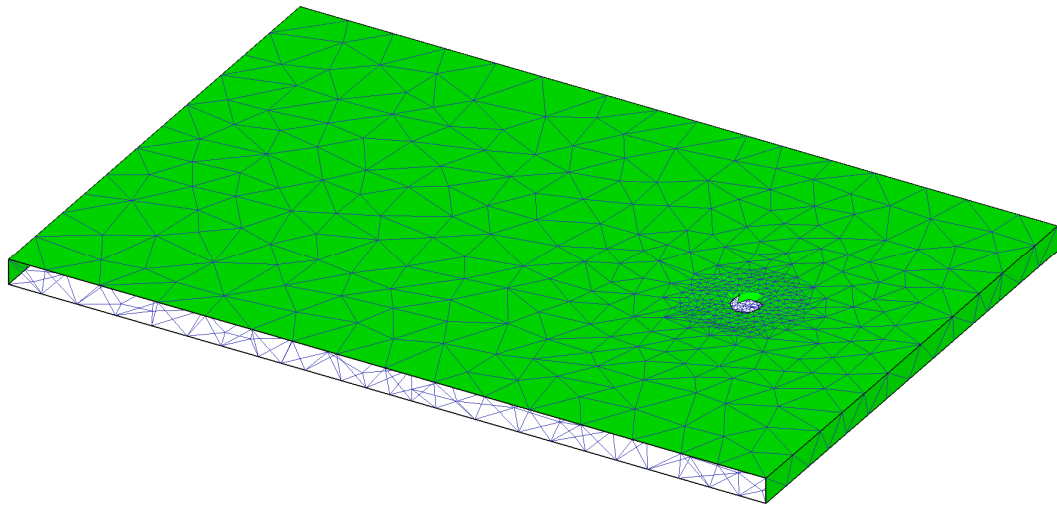


Figure 5: The workpiece surfaces defined with convection heat transfer

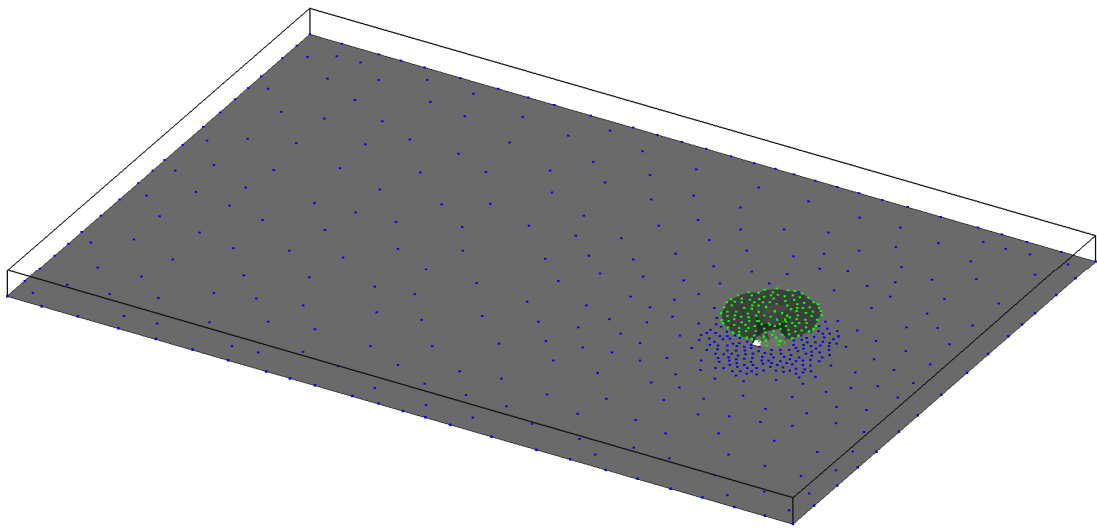


Figure 6: Conduction heat transfer condition at tool-workpiece interface (green nodes) and at the backing plate-workpiece interface (blue nodes).

6. Cooling Simulation

In the first cooling simulation, the work is proposed to be cooled via the backing plate where the coolant is pumped through channels fabricated through the backing plate which by itself cools the work placed above it (as per [67]). The temperature would be adjusted by controlling the flow of chilled water passing through the channels thus temperature can be set and maintained constant during the process. To approximate this in this FEM model, a constant temperature boundary condition was prescribed at the work lower surface. The nodes selected for this boundary condition are all the lower surface nodes of the workpiece which are in contact with the backing plate. It is important to note that using such a technique, the minimum temperature that can be achieved is 5°C which is equal to the prescribed temperature in the FEM model.

In the second cooling simulation, CO2 cryogenic cooling is modeled. In this cooling system a nozzle is placed where it trails behind the tool to where it follows the tool translational motion. Liquid CO2 is sprayed on the surface of the weld. The area subjected to cooling was chosen to be of a circular shape and to be slightly larger than the shoulder diameter and was located on the top of the work just behind the tool. This uniform heat flux was modeled as a convective heat loss problem as described by

$$\dot{q}_c = h_c (T - T_{\min}) \quad (4)$$

where

h_c convective heat transfer coefficient

T current temperature

T_{\min} minimum coolant temperature

The h_c value used was 2 N/(mm.s.C) (as derived experimentally by [60]) and -50°C for T_{\min} which is the boiling temperature of CO2.

7. Grain Size Prediction

The average grain size (D) can be calculated from the Zener-Hollomon parameter (Z) according to the linear relationship between $\ln(Z)$ and D as described by

$$D = \frac{1}{a + b \ln(Z)} \quad (5)$$

where

D average grain size

a, b AL7075 material constants [68]

The material constants of Equation 5 for the aluminum alloy AL7075 used for the workpiece in this model were taken from [68] and are shown in Table 4.

Z on the other hand is related to the strain rate ($\dot{\epsilon}$) and temperature (T) according to

$$Z = \dot{\epsilon} e^{\left(\frac{Q}{RT}\right)} \quad (6)$$

where

$\dot{\epsilon}$ effective strain rate

T absolute temperature

Q activation energy [68]

R universal gas constant

Table 4:AL7075 material constants used for Z (from [68])

Property	Value
Material constant a	-3.43 um^{-1}
Material constant b	0.162 um^{-1}
Activation energy Q	148 kJ/mol
Universal gas constant R	8.314 J/(kg K)

E. Magnesium Similar model

1. Parts and Meshes

A thermo-mechanically coupled model was implemented for modeling the friction stir welding with the different parts shown in Figure 7. The model comprises the tool, the workpiece, and the backing plate.

Both the tool and the backing plate were modeled as rigid un-deformable bodies where only heat transfer was accounted. As for the workpiece, it was modeled as a plastic body subject to both deformation and heat transfer.

The considered tool had an 18 mm cylindrical shoulder with a 6 mm diameter smooth unthreaded pin that extrudes 6 mm from the bottom of the shoulder. The tool was tilted 3° about the vertical axis in the processing direction to further improve material flow. Both the workpiece and the backing plate had an area of $80 \times 54 \text{ mm}^2$ and a height of 10 mm.

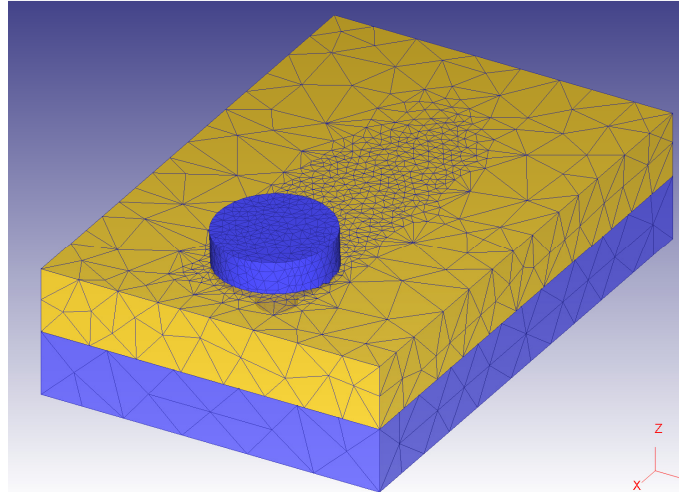


Figure 7: The meshed magnesium FEM model

Tetrahedral elements were used in the FEM model with active local re-meshing triggered by a relative interference ratio of 70% between contacting edges. This would ensure the integrity of the workpiece geometry during deformation.

The tool and the backing plate were meshed for thermal analysis purposes with each containing around 6000 and 5000 elements respectively while the workpiece had about 16000 elements. To further capture the state variables at the tool-workpiece interface, a rectangular mesh control window was applied around the processing area of interest where finer mesh elements were created.

2. Material Modeling

Materials used in the FEM model were H13 steel for the tool, AISI-1025 steel for the backing plate and AZ31b for the workpiece. Table 5 summarizes the different mechanical and thermal properties of AZ31b along with the material constants used. A rigid visco-plastic material model was used for the workpiece where the flow stress ($\bar{\sigma}$), temperature (T), and strain rate ($\dot{\epsilon}$) are coupled by Equation 7.

$$\dot{\epsilon} = A [\sinh(\alpha \bar{\sigma})]^n \exp[-\Delta H / (RT)] \quad (7)$$

Where A, α , and n are material constants, ΔH being the activation energy, and R the universal gas constant.

Table 5: Material properties of AZ31b used in the model

Property	Value
Elastic Modulus [69]	44830 MPa
Poisson's ratio [69]	0.35
Coefficient of thermal expansion [69]	2.65×10^{-5}
Thermal conductivity [69]	96 N/(s K)
Heat capacity [70]	2.43 N/(mm ² C)
Emissivity [70]	0.12
Material constant A [71]	27.5 s ⁻¹
Material constant α [71]	0.052 MPa ⁻¹
Activation energy ΔH [71]	130 kJ/mol
Material constant n [70]	1.8
Universal gas constant R [71]	8.314 J/(kg K)

3.

4. Friction Modeling

Friction at the tool-workpiece interface is a significant factor in any FSW simulation. It is reached that 86% of the heat generated is due to frictional forces [72].

Determination of the friction factor is a daunting challenge due to the variation of temperature, strain rate, and stress. Different literature publications investigated the value of friction coefficient in magnesium alloys [73-75]. Most authors use the ring upsetting and compressions tests for determining the coefficient of friction. It is agreed that the friction factor increases with temperature [76]. However, this increase of friction factor with temperature is valid until the liquidus temperature of AZ31b (630°C) is reached where the friction drops drastically. The values of experimental data [73] were entered to the model and then extrapolated by tuning different runs and analyzing state variables. The friction coefficient versus temperature used in the FE model is shown in Figure 8. This is based on experimental data [73] as well as on sensitivity analysis for model calibration as previously by the authors [76].

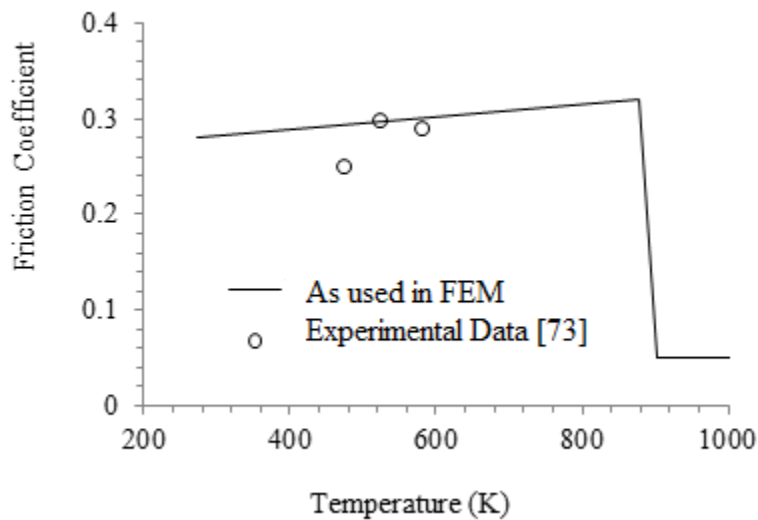


Figure 8: Friction coefficient vs. temperature as used in FE model; shown compared with experimental data [73]

5. **Boundary Conditions**

Heat transfer with the environment was accounted for all the three meshed objects with a convective heat coefficient of $20 \text{ W}/(\text{m}^2 \text{ }^\circ\text{C})$ at a constant temperature of 293K . The heat transfer coefficient between the tool-workpiece and backing plate-workpiece interfaces was set to $11 \text{ kW}/(\text{m}^2 \text{ }^\circ\text{C})$ [57].

Cooling was implemented to the FE model by applying a different convection heat coefficient to a circular area behind the tool traverse line. The cooled area was considered to be 16 mm in diameter to simulate air flowing from a compressed air-gun nozzle placed 5 cm above the workpiece. The air temperature was considered to be 293 K while the convective heat transfer coefficient was varied from 3 to $10 \text{ kW}/(\text{m}^2 \text{ }^\circ\text{C})$ to simulate different cooling rates.

The simulation time step selection should be optimized to prevent redundant calculations while preserving the state variables' accuracy. The time step in the simulation was calculated based on the tool rotational speed and the minimum element size to guarantee a calculation step every 5 degrees of the tool rotation. This would lead to higher simulation steps with higher tool rotational speeds.

Simulation time was further reduced by neglecting the plunging phase of FSW and taking into consideration the traversing phase alone. To account for the deformation produced by the plunging phase, the tool final plunged shape was cut from the

workpiece geometric model. A dwelling phase was added at the beginning of each run where the tool rotated in its place to raise temperature at the stir zone to the plunging elevated levels.

Since the traverse speed effects have minor effects when compared to those of the tool RPM [72], a constant traverse speed of 90 mm/min was used in the simulations with a trapezoidal speed profile that had a rise time of 0.5 sec. This would ensure a smooth processing start and prevent voids at the plunging region. The tool rotational speed, being the most affecting parameter, was varied over a range from 180 to 1800 RPM.

6. GrainSize Prediction

To evaluate the effect of optimized parameters, the average grain size (d) was calculated using equation 8 where Z is the Zener-Hollomon parameter and the constant values in the equation for AZ31 were obtained from the literature [77]. The Zener-Hollomon parameter is related to temperature and strain rate by equation 6 with Q being the activation energy and R the universal gas constant as per table 5.

$$\ln d = 9 - 0.27 \ln Z \quad (8)$$

For the sake of comparison with experimental values available in the literature, the material was assumed to have a starting average grain size of $8\mu\text{m}$. The microstructure was then updated as per equation 8 during the simulation.

F. Steel Model

1. Parts & Meshes

A thermo-mechanically coupled model using the FE software DEFORM was implemented to model the friction stir welding of carbon steel. As shown in figure 1, the model comprises the tool, the workpiece, and the backing plate. Also shown superimposed on the meshed geometry is a rendering of the in-process laser source. To model the laser source, a heat source circular window with constant heat flux was defined. The circular window is of diameter 2 mm and is placed 5 mm in front of the tool. The power of the laser was 2kW.

Both the tool and the backing plate were modeled as rigid un-deformable bodies where only heat transfer was accounted. On the other hand the workpiece was modeled as a plastic body subject to deformation and heat. The two plates to be welded were modeled as one block to avoid numerical instabilities at the contact.

The considered tool was a cylindrical shoulder 15mm in diameter. From the bottom of the shoulder, a 6 mm diameter smooth unthreaded pin extrudes 3.2 mm. The tool was tilted 3° about the vertical axis in the processing direction to further improve material flow. Both the workpiece and the backing plate had an area of 60x40 mm² and a thickness of 3.2 mm.

Tetrahedral elements were used in the FEM model. The tool and the backing plate were meshed for thermal analysis purposes only with each containing around 10000 and 5000 elements respectively while the workpiece had around 24000 elements. To further capture the state variables at the tool-workpiece interface, a rectangular mesh control window was applied around the processing area of interest where finer mesh elements (around 0.3 mm) were created as shown in Figure 9.

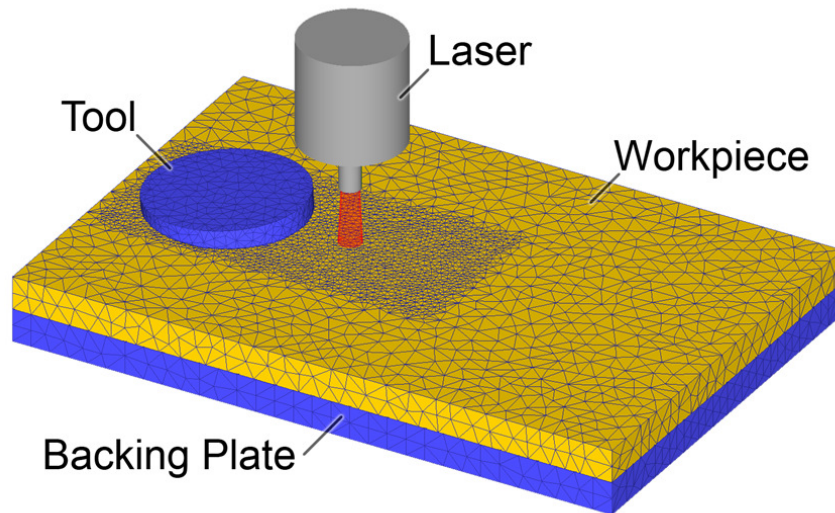


Figure 9: The meshed FE model showing the tool, workpiece, and backing plate (under the workpiece). Shown superimposed is a rendering of the in-process laser source.

2. Material Modeling

The material used for the tool and the backing plate was WC based alloy. As for the workpiece, it is believed that the final weld mechanical properties are strictly dependent on the volume fraction of phases present. Therefore, AISI 1045 (workpiece material) was defined as a mixture of phases. Specifically three phases were defined: martensite, austenite, and pearlite. The transformation to any of the phases was defined according phase transformation, isothermal, and continuous cooling transformation diagrams shown in Figures 10,11,12. The functions recommended by DEFORM are listed below in Table 6 and which were used along with the appropriate generated latent heat values. The initial volume fraction of the elements was defined as 100 percent pearlite which is predominantly the case of as received mild-carbon steels. Each phase has its own material properties which are, in turn, function of temperature. Similarly,

each of the phases has its own flow stress equation. The linear hardening equation used to formulate the stress equation was

$$\bar{\sigma} = Y(T, A) + H(T, A)\bar{\epsilon} \quad (9)$$

A = Atom content

T = Temperature

$\bar{\epsilon}$ = Effective plastic strain

$\bar{\sigma}$ = Flow stress

Y = Initial yield stress (temperature dependent)

H = Strain hardening (temperature dependent)

Table 6: Phase Transformation Models

Phase 1	Phase 2	Transformation Model
Austenite	Martensite	Magee's Equation
Austenite	Pearlite	Diffusion(TTT curve)
Martensite	Austenite	Diffusion(Simplified)
Pearlite	Austenite	Diffusion(Simplified)

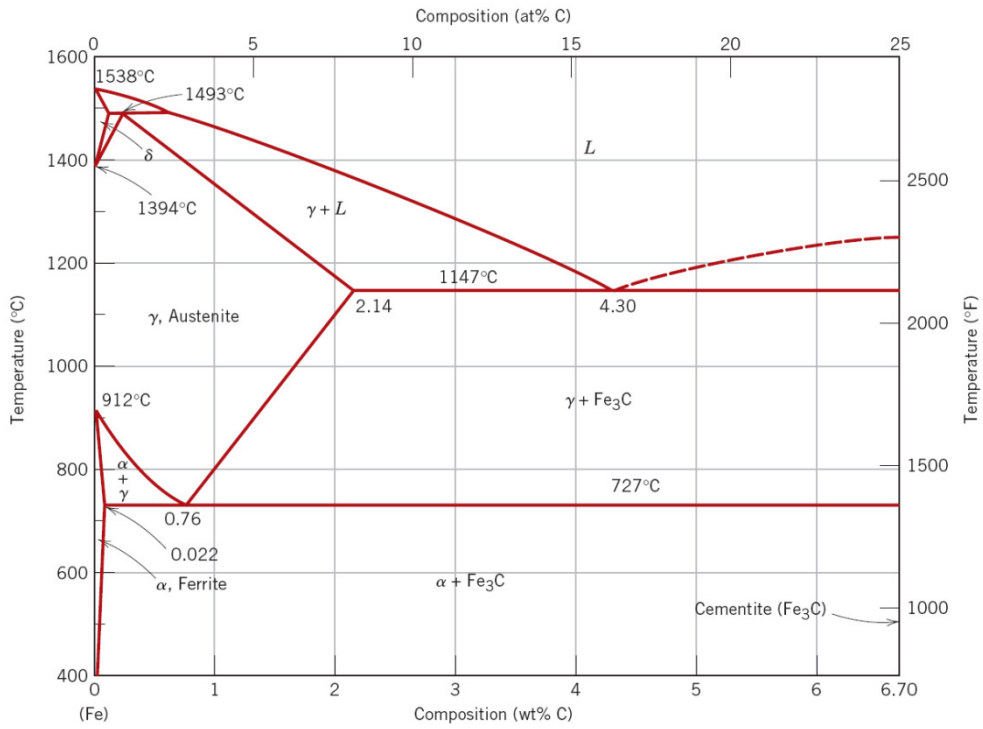


Figure 10: The iron-iron carbide phase diagram [78]

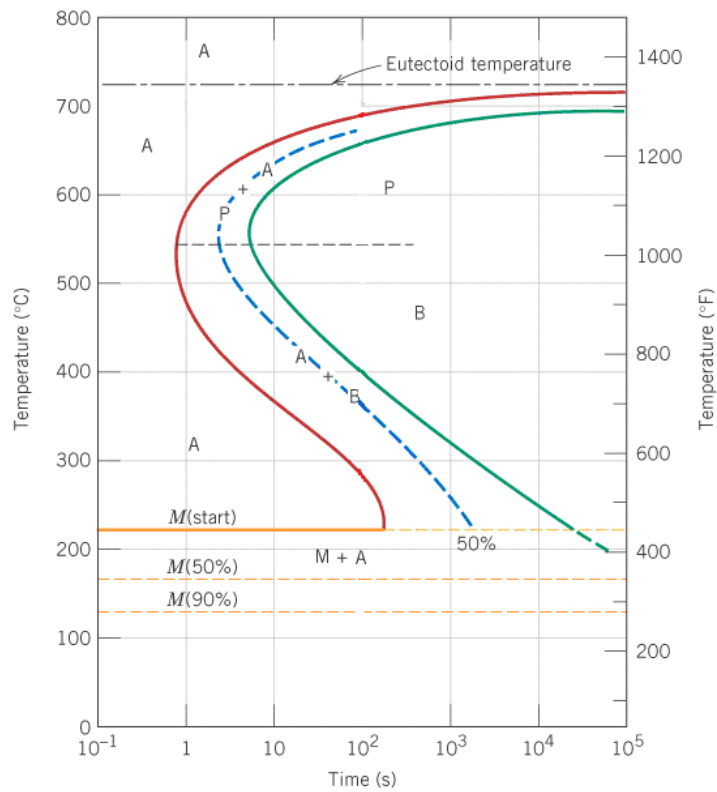


Figure 11: Isothermal transformation diagram of iron-carbon alloy of eutectoid composition [78]

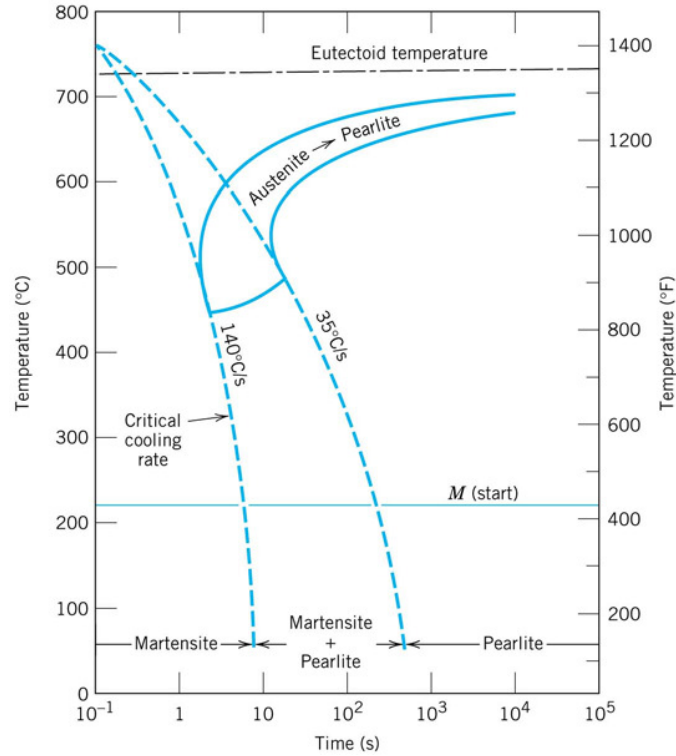


Figure 12: Continuous cooling transformation diagram of eutectoid iron-carbon alloy [78]

3. Friction Modeling

Friction at the tool-workpiece interface is a very complex process due to the variation of temperature, strain rate, and stress which make friction modeling a difficult technique. In [79], a numerical model with experimental evidence was developed to estimate the shear friction coefficient in FSW. The model uses the tool speed and dimensions to estimate the shear friction coefficient as shown below:

$$\mu_f = \mu_0 \exp(-\lambda \delta \omega r) \quad (10)$$

Where δ is the percentage sticking and r is the radial distance from the tool axis for the point in consideration. The values of constants were used as follows: $\mu_0= 0.4$, $\delta= 0.4$, $\omega=62.8$ radians, $r= 0.003\text{m}$ and constant λ was 1s/m [80].

4. **Boundary Conditions**

Heat transfer with the environment was accounted for the three meshed objects (tool, workpiece, and backing plate) via a convective heat coefficient of $20 \text{ W}/(\text{m}^2 \text{ }^\circ\text{C})$ at a constant temperature set at 293K for the surrounding environment. The heat transfer coefficient between the tool-workpiece and the backing plate-workpiece interfaces was set to $11 \text{ kW}/(\text{m}^2\text{ }^\circ\text{C})$. Local re-meshing was triggered by a relative interference ratio of 70% between contacting edges. This would ensure the integrity of the workpiece geometry during deformation. The simulation time step selection should be optimized to prevent redundant calculations while preserving the state variables' accuracy. The time step in the simulation was determined based on the tool rotational speed and the minimum element size to guarantee a calculation step every 5 degrees of the tool rotation. Simulation time was further reduced by neglecting the plunging phase of FSW and taking into consideration the traversing phase alone. The tool final plunged shape was cut from the workpiece geometric model to account for the deformation produced by the plunging phase. A dwelling phase was added at the beginning of each run where the tool spins in its place to raise the temperature at the stir zone to the plunging elevated levels. In tool movement definition, a trapezoidal speed profile with a rise time of 0.5s was used. This would ensure a smooth processing start and prevent voids during the plunging stage.

G. Aluminum Magnesium Dissimilar Model

1. Parts and Meshes

To simulate DFSW, a thermo-mechanically coupled model was implemented using DEFORM 3DTM (Scientific Forming Technologies Corporation, 2545 Farmers Drive, Suite 200, Columbus, Ohio 43235). As shown in Figure 13, the model is comprised of the tool, the workpiece (top), and the backing plate (located under the work). Both the tool and the backing plate were modeled as rigid un-deformable bodies where only heat transfer was accounted for. The two plates to be welded were modeled as a single block to avoid numerical instabilities at the contact region. This workpiece was modeled as a visco-plastic body subject to both deformation and heat transfer.

The considered tool consisted of a 20 mm diameter cylindrical shoulder and a 7 mm diameter pin that extrudes 2.8 mm from the bottom of the shoulder. The tool was tilted 3° about the vertical axis in the welding direction to further improve material flow. Both the workpiece and the backing plate had an area of $50 \times 60 \text{ mm}^2$ with a thickness of 10 mm.

Tetrahedral elements were used in the model with active local re-meshing triggered by a relative interference ratio of 70% between contacting edges. The tool and the backing plate were meshed for thermal analysis purposes with each containing around 5000 and 8000 elements respectively while the workpiece had initially around 70000 elements. In any FE, model the number of elements used directly affects

simulation time while the size of elements used affects results accuracy. Therefore, to accurately capture state variables with minimum simulation times, three refinement windows were used at area of interest. The first window was set at the tool-workpiece interface (average element size of 1 mm). The second window was added at the interface between the two elements (average element size 0.1 mm). This window should have such small elements since the very thin intermetallic compounds are expected to form in this area. The third window was added at the pin of the tool in such a way the size the elements at the pin matches the sizes of elements at the workpiece to achieve better contact calculations. The simulation time step selection should be optimized to prevent redundant calculations while preserving the state variables' accuracy. The time step in the simulation was calculated based on the tool rotational speed and the minimum element size to guarantee a calculation step every 5 degrees of the tool rotation. Simulation time was further reduced by neglecting the plunging phase of FSW and considering the traversing phase alone. To account for the deformation produced by the plunging phase, the tool final plunged shape was cut from the workpiece geometric model. A dwelling phase was added at the beginning of each run where the tool rotated in its place to raise temperature at the stir zone to the plunging elevated levels. All the process parameters such as rotational speed, linear feed, dwelling time and some other geometric parameters were set as per the experiment to be compared against as will be stated below.

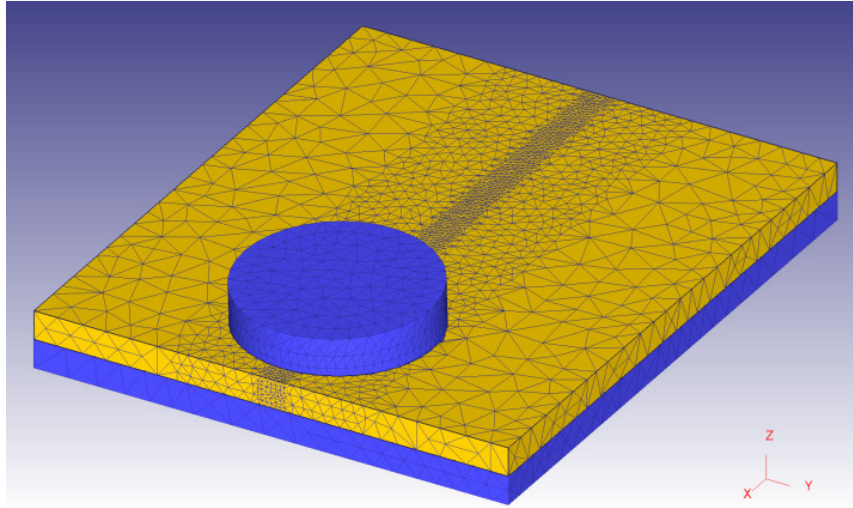


Figure 13: The mesh of the tool, backing plate, and workpiece for the Al/Mg Model

2. Material Modeling

The material used for the tool and backing plate was steel H13 steel. As for the workpiece, it is believed that during welding both mixing and phase transformations between aluminum and magnesium will take place. Accordingly, a new material had to be defined in DEFORM as a mixture of the two parent phases, aluminum and magnesium. At the beginning of the simulation the elements at the advancing side were set to have a volume fraction composition of 100% aluminum while the retreating side elements were set to be 100% magnesium as shown in Figure 14.

The material properties and flow stress equations for each of the phases (Aluminum/Magnesium) were defined separately. The Aluminum used was Al5083 while the magnesium used was AZ31b. A rigid visco-plastic material model of the form

$$\bar{\sigma} = \frac{1}{\alpha} \sinh^{-1} \left[\frac{1}{A} \dot{\epsilon} e^{\left(\frac{Q}{RT}\right)} \right]^{\frac{1}{n}} \quad (11)$$

was used for both materials where flow stress ($\bar{\sigma}$), temperature (T), and strain rate ($\dot{\epsilon}$) are related by where A, α , and n are material constants, Q being the activation energy, and R the universal gas constant. Table 7 summarizes the different mechanical and thermal properties of both materials along with the material constants used.

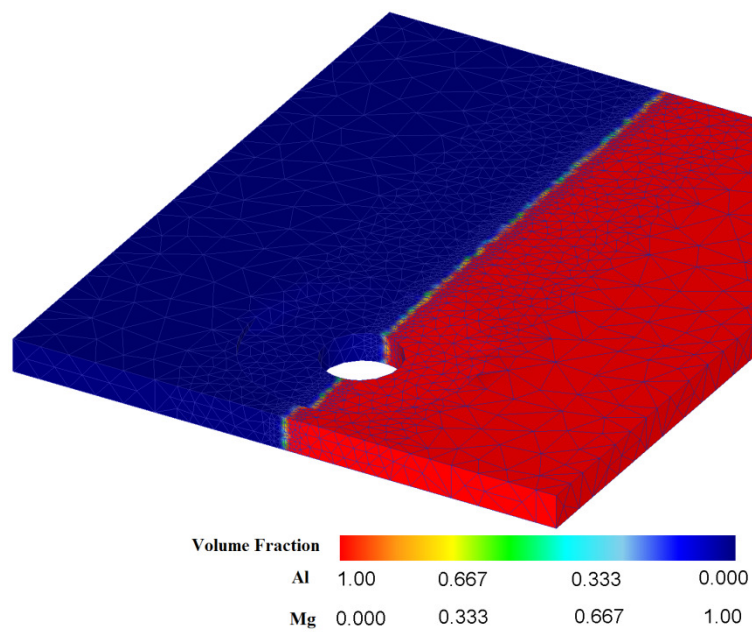


Figure 14: The volume fractions of elements at initial step

Table 7: Al and Mg material properties and constants summary

Property	Mg AZ31b	Al 5083
Elastic Modulus MPa	44830 [69]	68900 [81]
Poisson's ratio	0.35 [69]	0.33[81]
Thermal expansion coef.	2.65e-5[69]	2.34[81]
Thermal conductivity N/(s K)	96 [69]	120[81]

Heat capacity $N/(mm^2 C)$	2.43 [70]	2.433
Emissivity	0.12 [70]	0.7
Material constant $A s^{-1}$	27.5 [71]	1.088
Material constant αMPa^{-1}	0.052 [71]	0.0109[82]
Activation energy $\Delta H kJ/mol$	130	159969[82]
Material constant n	1.8 [71]	5.995[82]
gas constant $R J/(kg K)$	8.314 [71]	8.314[82]

3. *Friction Modeling*

Friction at the tool-workpiece interface is a very complex process due to the variation of temperature, strain rate, and stress which make friction modeling a difficult technique. Moreover, the dissimilar nature of the weld adds more complexity because each material may has its own friction coefficient.

Equation 10 was used and the values taken were as follows: $\mu_0= 0.4$, $\delta= 0.4$ while constant λ was $1s/m$ [13]. The value of the friction of coefficient was calculated and implemented accordingly. Moreover, the friction coefficient was reduced to about 0.02 when temperature reaches melting levels of temperature as mentioned before.

4. *Separation Criterion*

In FSW processes it is believed that the workpiece material movement does not exactly follow the tool movement (perfect sticking). Instead, particles in the work are continuously facing contact and separation conditions with the tool. Therefore, modeling the contact between the tool and the workpiece is a challenging task and

realistic assumptions must be taken into consideration. According to the DEFORM manual, the nodes on the workpiece are considered in contact with the tool if the force on the nodes is less than a predefined separation pressure. To calculate this value we used generic FSW compressive force range (10-20 KN) for our tool dimension and divided it by area (80 mm²) and an initial value of 150 was used as a separation criteria. This value was further tuned to 200 so that the state variables reflect the expected process behavior.

5. *Boundary Conditions*

Heat transfer with the environment was accounted for all the three meshed objects with a convective heat coefficient of 20 W/(m² °C) at a constant temperature of 293K. The heat transfer coefficient between the tool-workpiece and the backing plate-workpiece interfaces was set to 11 kW/(m² °C).

CHAPTER IV

MODEL VALIDATION AND RESULTS

H. Aluminum Similar Model

1. *Model Validation*

Validating the FEM model was accomplished by comparing its output with previously published experimental work [57]. The first validating criterion was the temperature history of a monitoring point (a node 8-mm away from the weld line). The results in Figure 15 show very good agreement with the experimental work by [57]. The figure shows the plot of the variation of temperature of the monitoring point for a period of 3.5 seconds. It is worth mentioning that the time shown on the x-axis is that of relative (welding) time. In Figure 16, a temperature contour for the workpiece is presented. The maximum temperature in the contour which is around the pin is higher than the validation maximum temperature. This is expected for the fact that the validation points were 8mm away from the pin thus it is not inside the stir zone. In Figure 18, a section parallel to the weld line on the advancing side of the pin was considered and temperature as the tool commences was monitored. It is clear from the figure how temperature slightly increases as the tool pass. Moreover, the temperature under the shoulder is the highest and decrease as we move away which is expected due to the surface friction effect. It is worth mentioning that this section is taken 1 mm away from the pin.

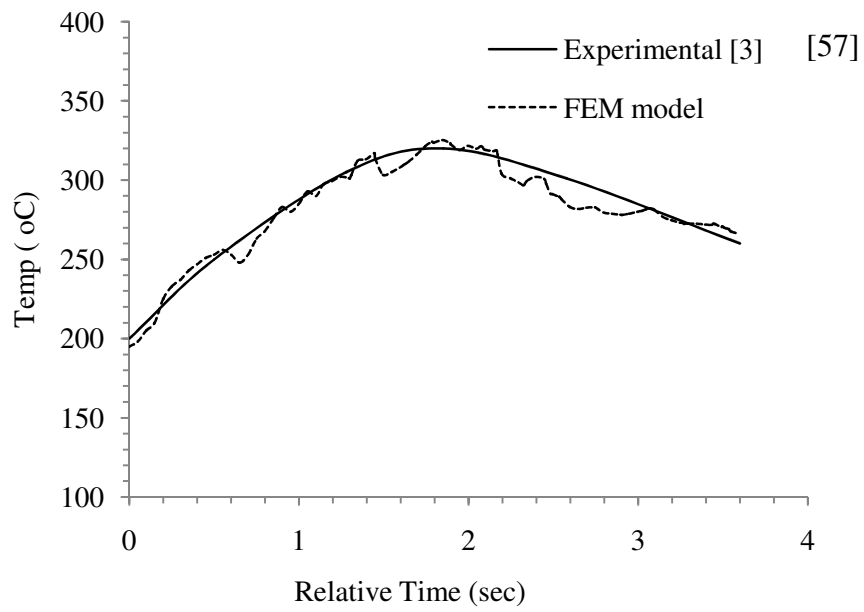


Figure 15: Temperature history of a node 8mm away from the weld line for a period of 3.5 seconds

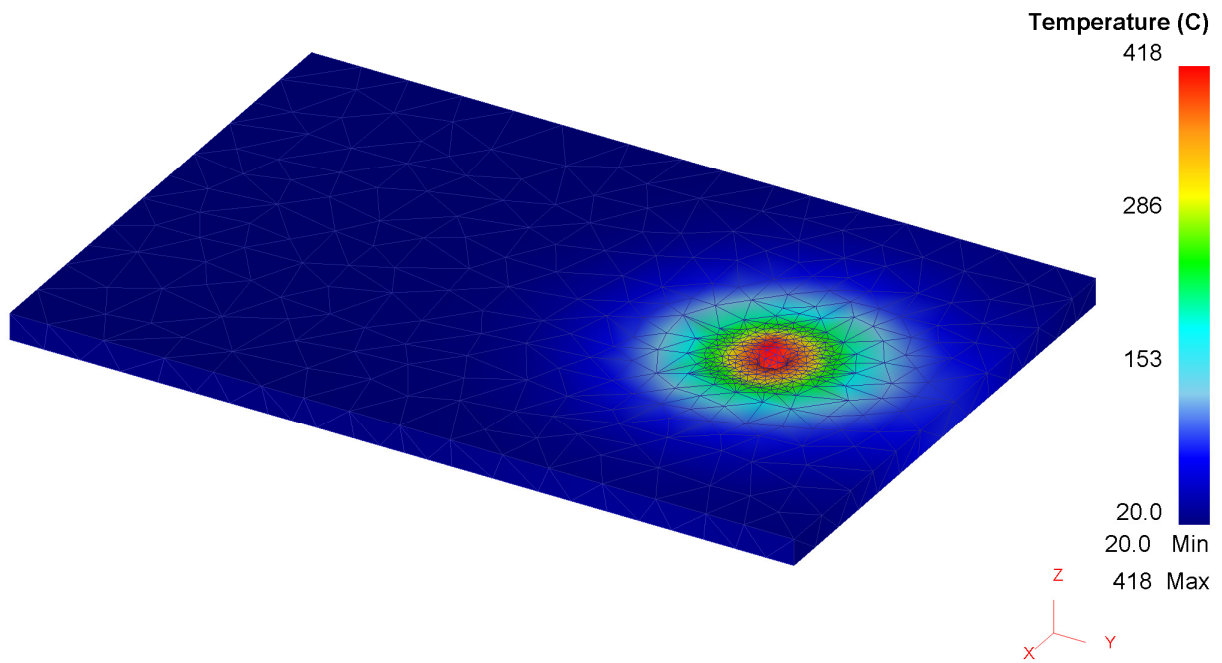


Figure 16: Temperature Contour in the workpiece

The second validating criterion was the grain size distribution across the weld line's cross section. Figure 18 shows a longitudinal grain size distribution for a distance of 2 mm from each side of the weld line. The figure shows good trend for the grain size as compared with the experimental results reported in [59].

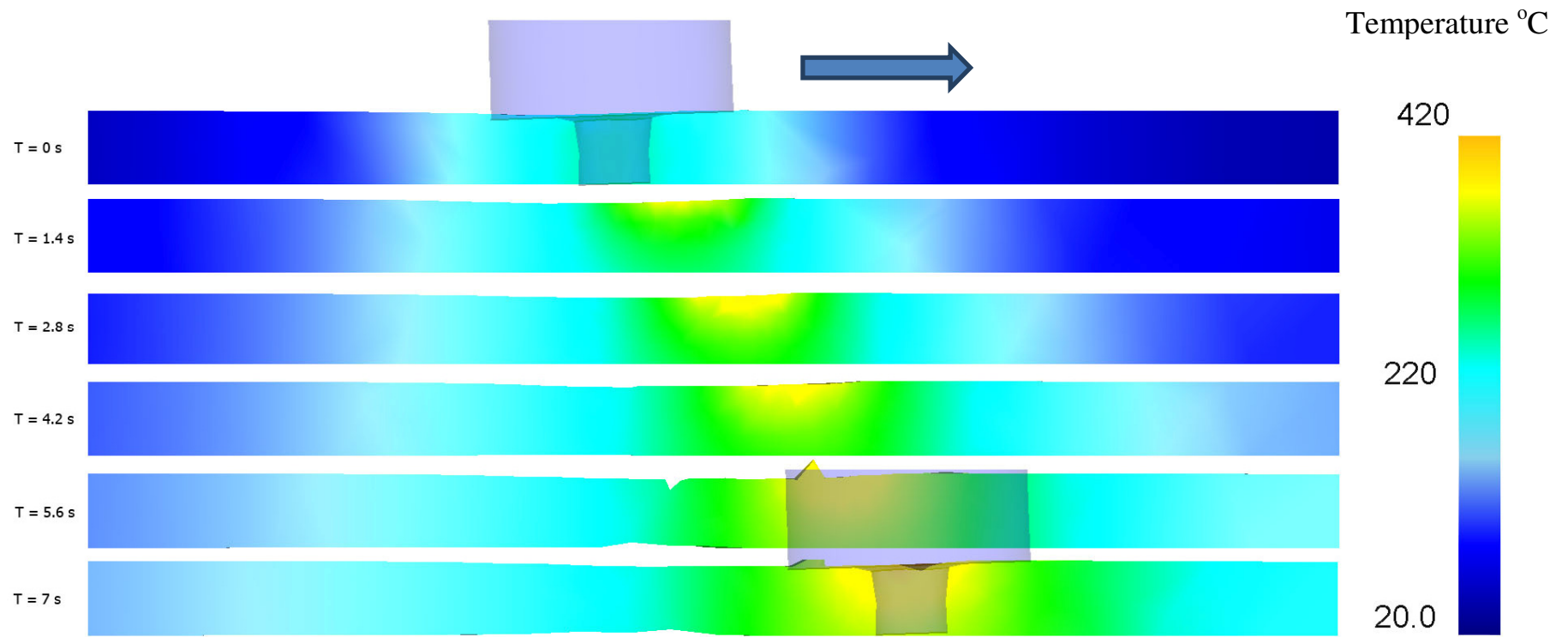


Figure 17: Temperature distribution for a section parallel to the weld line on the advancing side of the pin as the tool commences

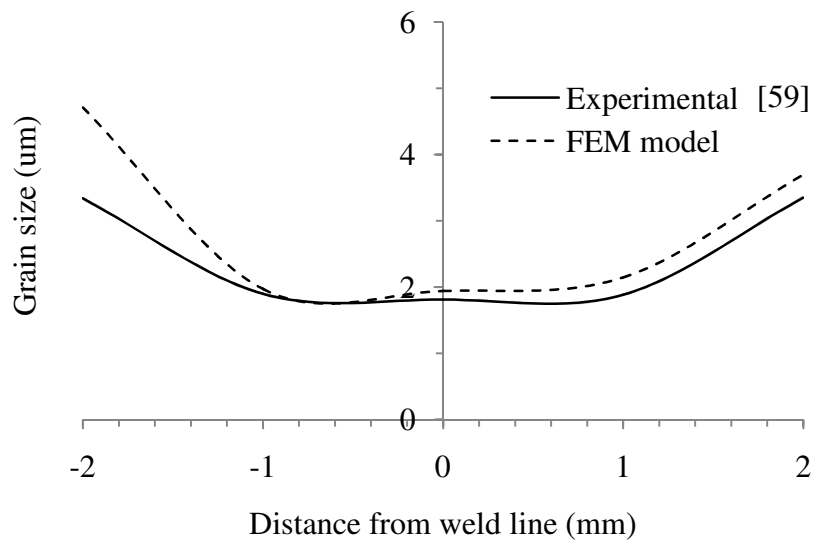


Figure 18: Grain size distribution across the weld line

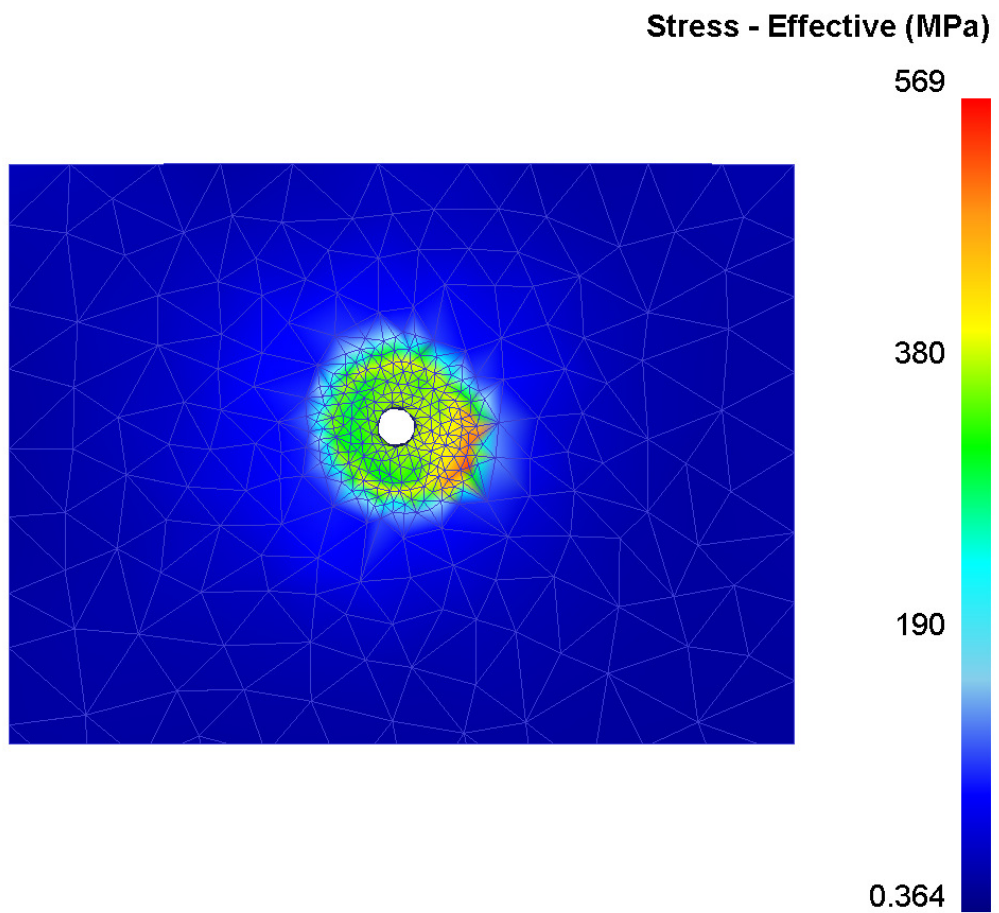


Figure 19: Effective stress distribution around welding area right after the dwelling phase

2. *Stress Distribution*

The stress distribution is an important factor to monitor in any FSW process. The stresses give an indication of the forces that need to be exerted by the machine during welding. In Figure 19, the effective stress which was extracted from DEFORM was plotted. It is clear in the contour plot how the stress is highest at the stirring area (around 300 MPa). It is worth mentioning that this plot was taken right after the dwelling phase in which after this step (during welding) the stresses stayed in the same range.

3. *Effect of Cooling*

Having arrived at good verification for the non-cooled, base case, the effect of both cooling techniques was then explored with the results shown in Figures 20 and 21. Figure 20 shows a minor effect of the first cooling scenario (through the backing plate) when compared with the cryogenic cooling scenario. Since the backing plate is maintained at 5°C from the opposite side of the weld, its conductive effect would be relatively small and can be clearly seen through a correspondingly small drop in the grain size. This effect was noticed to be more on the sides as one would move away from the weld line. On the contrary, cryogenic cooling is found to be more effective due to the close proximity of the cooling nozzle to the weld line in addition to the large values of heat transfer coefficients as well as the low value of the CO₂ reference cryogenic temperatures. A similar conclusion is drawn from Figure 21 which plots the distribution of $\ln(Z)$ across the weld line for both cooling techniques as well as the base case (no-cooling).

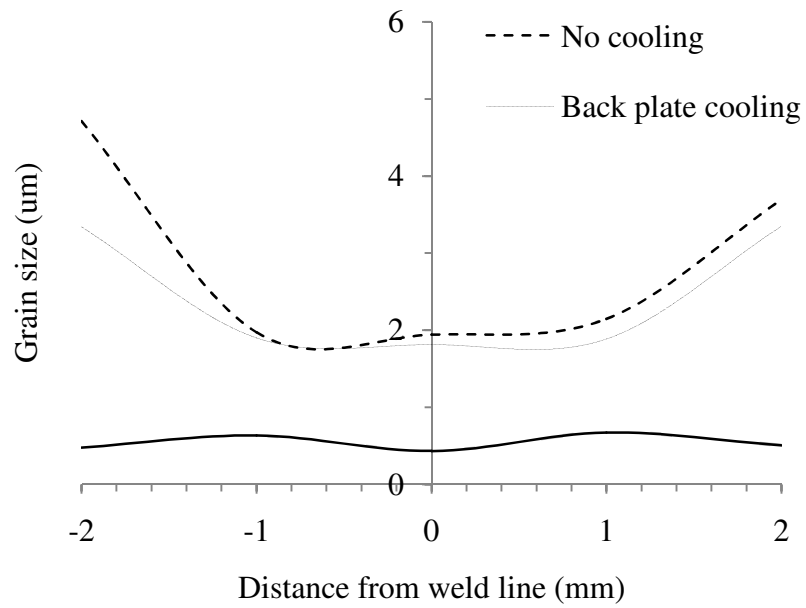


Figure 20: Distribution of the grain size across the weld line for: no cooling, back plate cooling, and CO2 cooling.

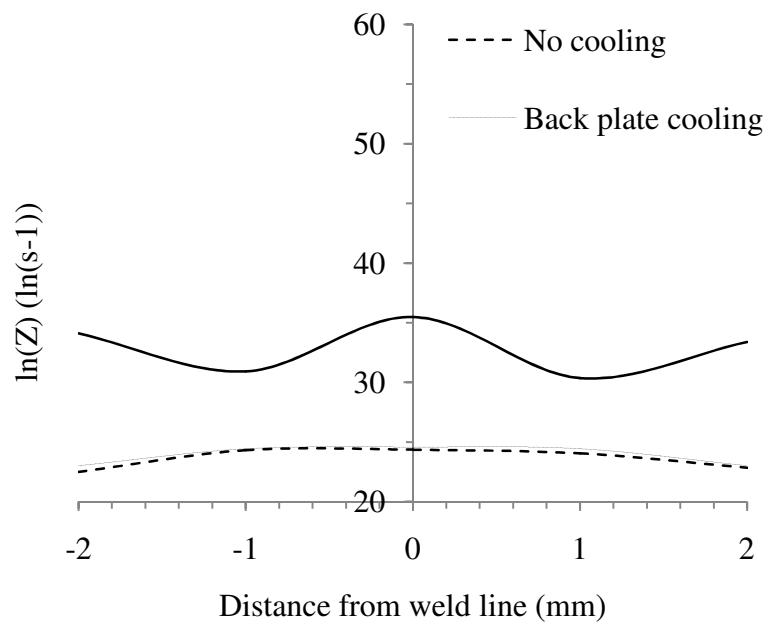


Figure 21: Distribution of $\ln(Z)$ across the weld line for: no cooling, back plate cooling, and CO2 cooling.

The cryogenic effect on the other hand, had a major influence all across the weld line. It can be noticed that nano-particles were formulated in the cooled area. This is due to the freezing-effect that captures the dynamic recrystallization effect and prevents the undesirable grain growth.

I. Magnesium Similar Model

1. *Model Validation*

The FEM model was validated with experimental data available in the literature by tracking the temperature history of an observation point on the traverse line at a distance of 8.5 mm from the surface for two different test cases. The processing parameters of these cases are described in Table 8.

Table 8: Processing parameters of the validation test cases

Property	Case 1	Case 2
Rotational speed (RPM)	800	1400
Traverse speed (mm/min)	90	90

Figures 22 and 23 shows a comparison between the simulated temperature histories and experimental results obtained from the literature [77]. The two figures

reflect the good accuracy of the presented FE model with the simulated data almost matching the experimental one.

The slight deviation in the temperature slope at the beginning of the curve is due to the steep temperature rise caused by the tool dwell in the simulation whereas in the experimental runs the temperature increased slower due to pin approach. The time scale in both figures was shifted to compensate for the difference between the experiment time and the FE simulation.

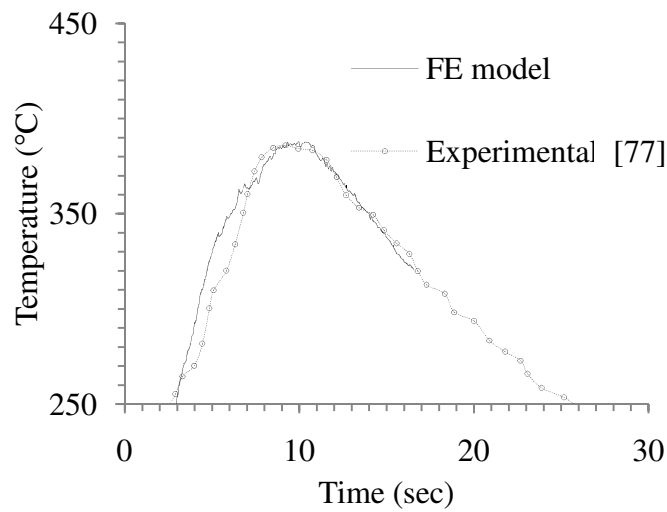


Figure 22: Experimental vs. simulated temperature profiles for the case 1 described in Table 8

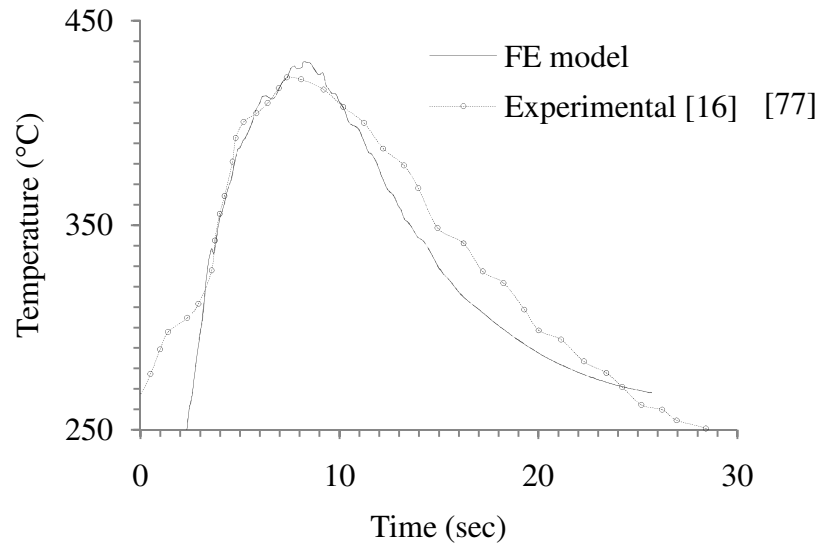


Figure 23: Experimental vs. Simulated temperature profiles for the case 2 described in Table 8

2. *Temperature Profile*

To fully illustrate the temperature distribution during the FSW of magnesium a temperature contour section of the weld is necessary. In Figure 24, a section of the perpendicular to the weld-line was considered to plot the temperature distribution. We can observe from this plot how temperature is maximum at the interface between the tool and the workpiece. This is expected because the friction between the two parts is the main source of heat. In the same plot we can observe how the generated heat is being conducted to the rest of the workpiece, backing plate and the tool. Moreover, a tracking point was selected to monitor the temperature as the tool passes. Conclusion similar to before can be reached.

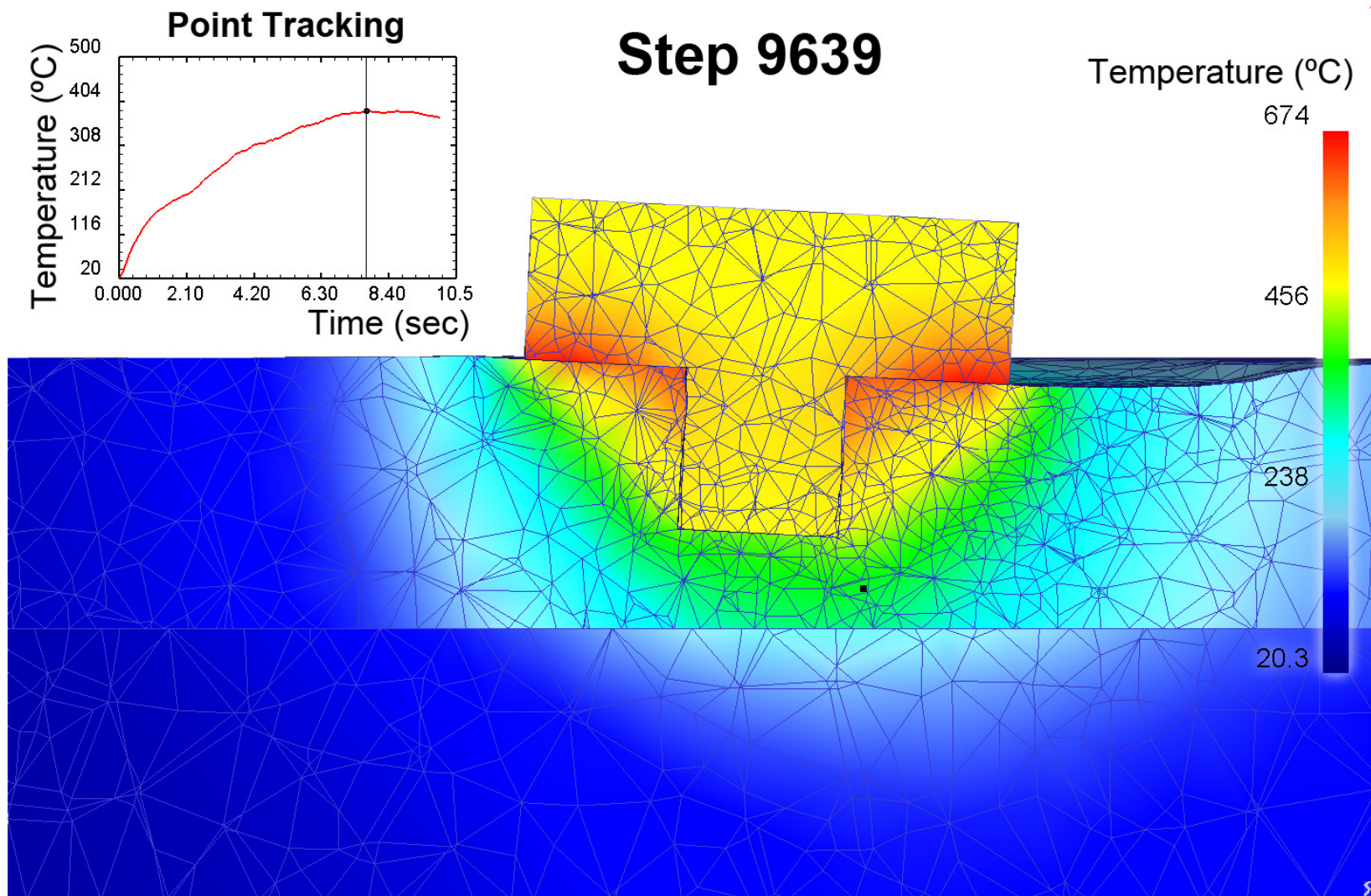


Figure 24: Temperature distribution along the weld section in the Mg model

3. *Effect of the Spindle Speed*

To find the optimum process parameters for friction stir processing of AZ31b at a constant traverse speed of 90 mm/min, the tool RPM as well as the cooling conditions were varied according to Table 9.

Table 9: Test cases at a traverse speed of 90 mm/min

Rotational Speed RPM	Cooling condition kW/(m ² °C)
160	3
600	5
800	10
1000	
1200	
1400	

For each convective heat coefficient listed in Table 9, the rotational speed was varied from 160 to 1800 RPM and the state variables were calculated. The corresponding average grain size was calculated according to equations 6 and 8 for top, middle, and bottom of the stir zone. The maximum reached temperature was reported as well to check if material melting is taking place.

Varying the spindle speeds resulted in major effect on the average strain rate, the maximum measured temperature and the corresponding average grain size. The actual strain

rate in friction stir welding was reported by several authors with ranges varying according to the proposed method of calculation.

In a recent publication that studied the effects of coolant applications in Friction stir processing using CFD analysis, strain rates of ranges 10^2 - 10^4 were calculated [67]. The same author argued about strain rate ranges of 10^0 - 10^2 that were previously obtained by researchers using equation 12 [77]. The model used in this manuscript confirmed the validity of equation 12 over the CFD analysis and Figure 25 backs up this confirmation.

$$\dot{\epsilon} = \frac{R_m \cdot 2\pi r_e}{L_e} \quad (12)$$

Where

R_m: the tool rotational speed

R_e: effective radius of the dynamically recrystallized zone

L_e: effective depth of the dynamically recrystallized zone.

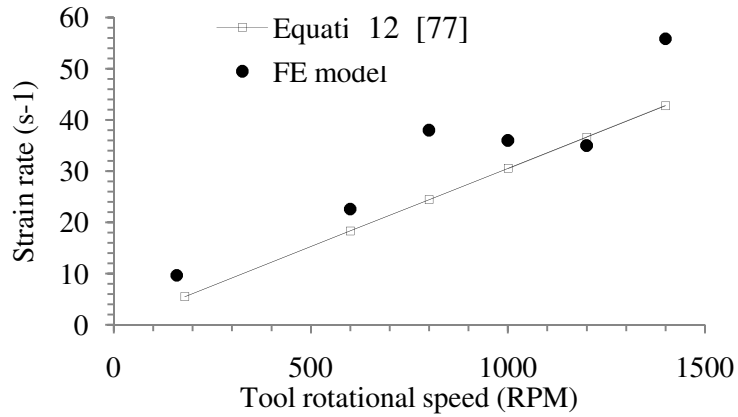


Figure 25: Variation of strain rate as function of tool rotational speed compared with results from equation 9

Different researchers found that the tool rotational speed had the most effect on the process temperature [83]. The variation of the temperature of the monitoring point previously described with the tool rotational speed is shown in Figure 26.

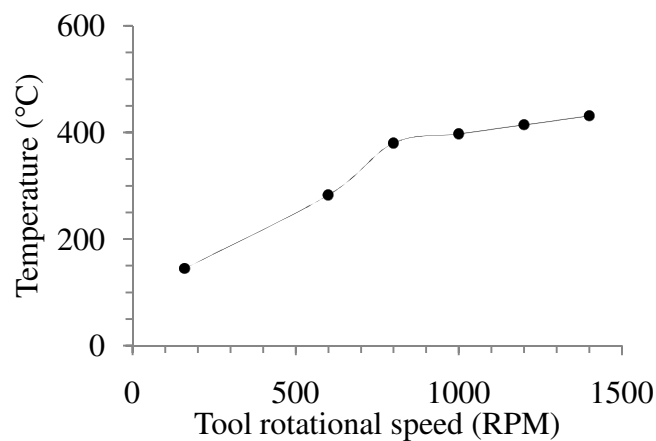


Figure 26: Variation of the maximum temperature of the observation point as function of tool rotational speed

The temperature at the observation point, which had a rough 200 °C difference from the upper processing zone, increased with the rotational speed as expected. However, when the temperatures of the processing zone approached the melting point of magnesium alloys (605-630 °C [67]) the coefficient of friction decreased and prevented further temperature increase resulting in the plateau shown in Figure 26.

The stir zone microstructure which is subject to dynamic recrystallization (DRX) was calculated based on equations 6 and 8. It was found that grain size varied with the depth from the top surface of the workpiece where smaller particles were found at the bottom. For example, the grain sizes for the top, middle, and bottom of the stir zone for the test conditions of case 2 in Table 8 were 7.95, 5.18, and 3.68 μm respectively compared to 8.1, 5.3, and 4.8 μm obtained by [77]. It was found that the average grain size throughout the processing zone increased with the tool rotational speed as shown in Figure 27.

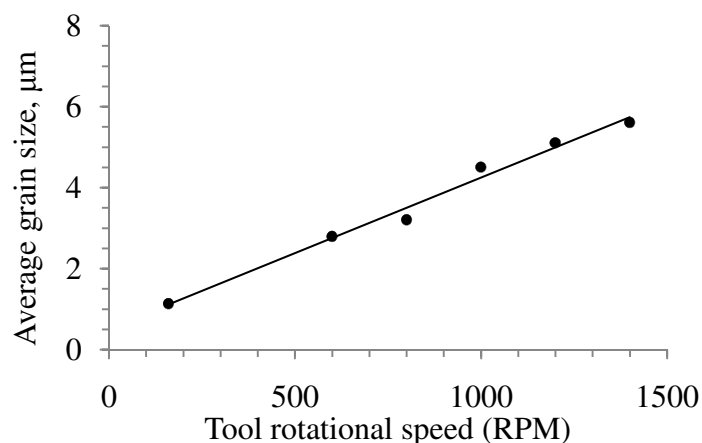


Figure 27: Variation of the average grain size as function of the tool rotational speed obtained from the FE model

4. *Effect of Cooling Rate*

The cooling conditions for the process were varied according to the cases described in Table 9. Varying the convective heat coefficient of the prescribed zone reflects to changing the flow rate of the coolant being utilized. It was noted for 3 different cooling condition cases that minor effects were observed at low tool rotational speeds. This is likely due to the low temperature gradient at low speeds which results in less observable effects. Minor temperature variations were found at the observation point due to its position far from the area being cooled. The effects were more obvious on the average grain size as shown in Figure 28.

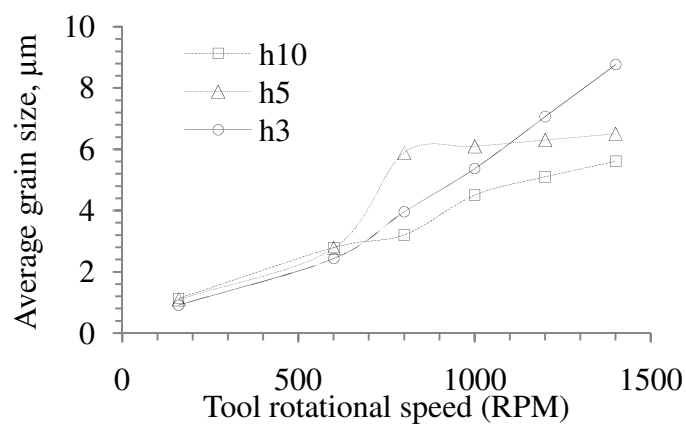


Figure 28: Variation of the maximum average grain size with the tool rotational speed for different cooling conditions

The average grain size had a trend that decreased with the increase of the convective heat coefficient were h10, h5, and h3 described in Figure 28 corresponds to the cooling conditions described in Table 9.

J. Steel Model

1. *Model Validation*

The FEM model was validated against experimental data available in the literature by tracking the temperature history of an observation point at the seam line at a distance of 0.5 mm above the shoulder for two different test cases. The processing parameters of both cases are described in Table 10.

Table 10: Processing parameters of the validation test cases for steel model

Property	Case 1	Case 2
Rotational speed (RPM)	600	600
Traverse speed (mm/min)	100	400

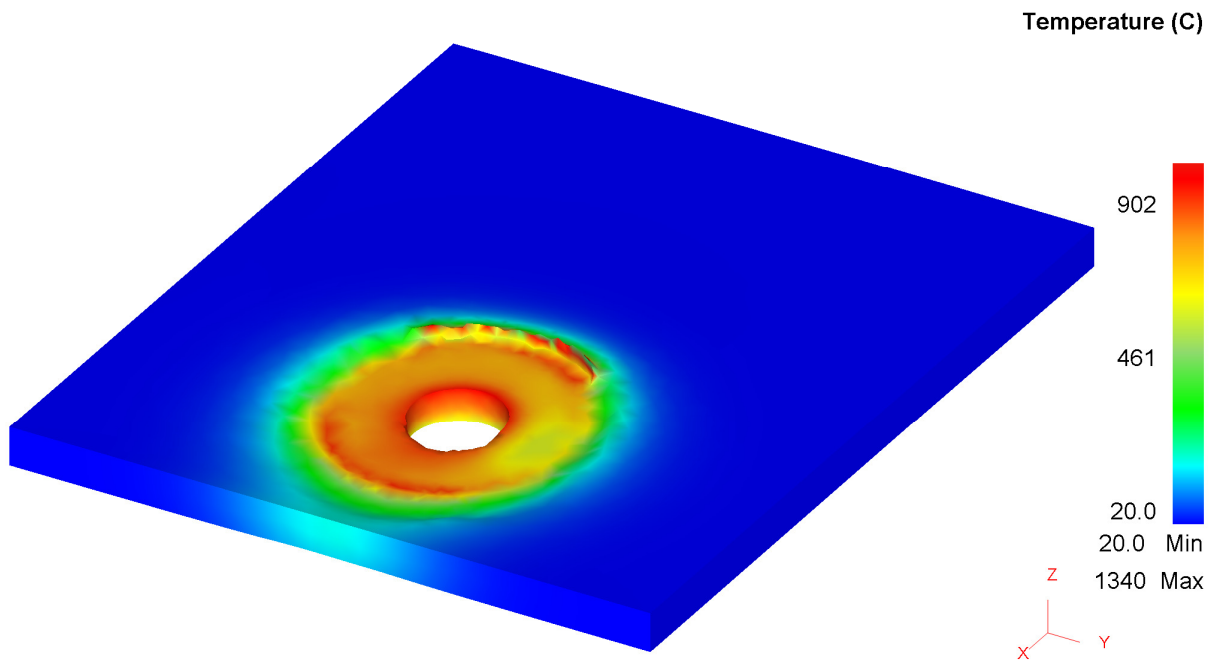


Figure 29: Temperature contour plot in workpiece for case 2

Figure 29 shows the temperature contours for case 2 (rotational spindle speed = 600 rpm, traverse speed = 400 mm/min) where peak temperature is located at the pin/tool interface as one would normally expect in an FSW process.

Plotted in Figure 31 are the simulated temperature profiles versus time for 2 cases: normal FSW and laser-assisted FSW. Co-plotted are the peak temperatures measured in [24]. It can be seen from the Figure that the peak simulated temperature is very close to the experimentally measured maximum temperature for case 2 for both cases: normal FSW and in-process laser assisted FSW.

Another comparison is made in Figure 31 where the peak temperatures for rotational spindle speed = 600 rpm are plotted against traverse speed at 100 and 400 mm/min. The results show good agreement was reached with the experimental results [24]. Figures 30 and 31 constitute the model validation phase in this work.

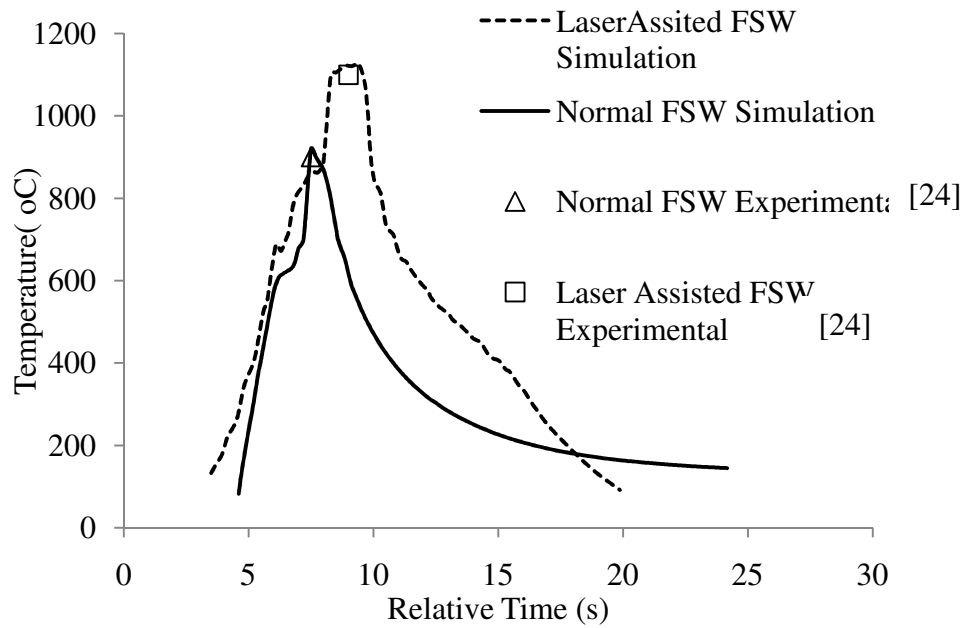


Figure 30: Simulation Temperature Profile with experimental [24] peak temperature for case 1

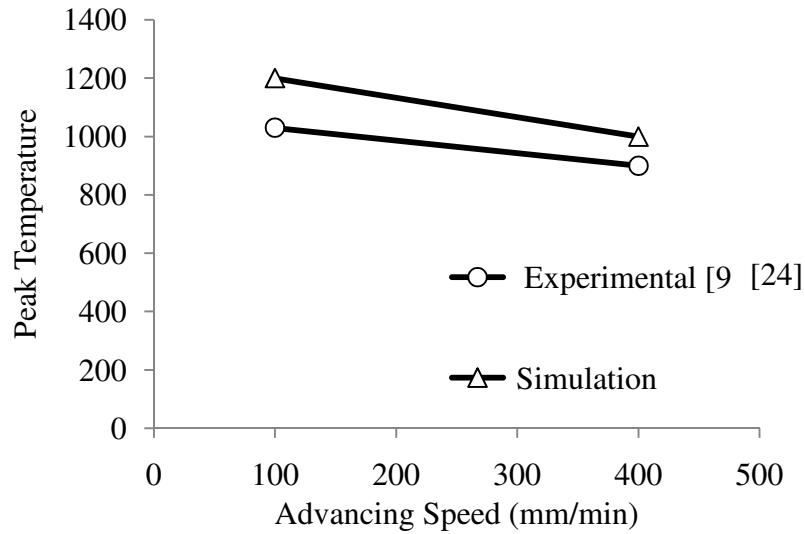


Figure 31: Peak temperatures versus advancing speed for experimental [24] and simulation test cases

2. *Effect of advancing speed on temperature*

The effect of the tool advancing speed on the weld temperature was studied. It was found that as the advancing speed increases the welding temperature decreases. This trend was reached experimentally and from the simulation as shown in Figure 31. Furthermore, this decrease of temperature with advancing speed increase is expected since at lower advancing speed more heat is generated with lower cooling rate.

3. *Strain Distribution*

Another important parameter extracted from the developed FE model was the effective strain. It is shown from Figure 32 that the strain reaches maximum value at the weld center and decreases as we move away from the weld line. Moreover, the strains on the advancing side of the weld are a bit higher which proves the non-symmetry property of the

FSW welds. Moreover, also from Figure 32, the value of the strain decreases with increasing advancing speed. This is expected since at lower advancing speed more time is given for stir action thus increasing plastic deformations resulting in strain increase.

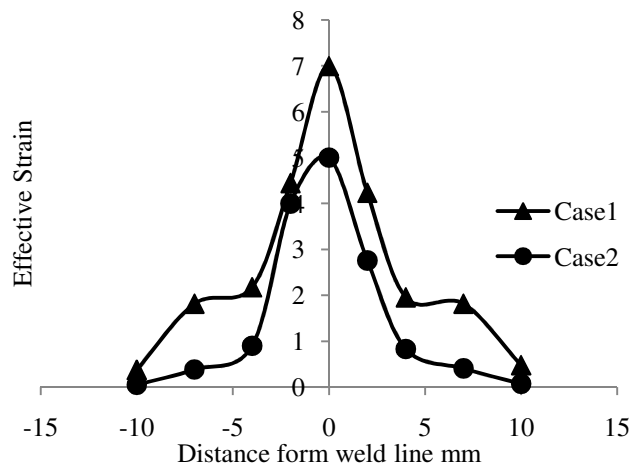


Figure 32: Effective strain distribution across the weld section for both test cases

4. *Phases Transformation*

The resulting mechanical properties of carbon steel joints ultimately depend on the intermetallic phases present and, thus, on the heating and cooling histories during the process. During FSW of carbon steels, temperature exceeds the transition temperature (about 727 °C for many steels) at which austenite begins to form upon heating. Therefore, transformations from austenite to other forms such as pearlite, martensite, and bainite will take place afterwards. Furthermore, the amount and type of these transformations is directly affected by the maximum temperature (mostly related to rotational speed) and cooling rate (mostly related to advancing speed). Other external heating (e.g., laser) and cooling (cryogenic) sources during FSW/FSP also play a critical role in altering these phase transformations and the resulting grain size for many materials.

In this work, modeling of phase transformations was made possible in DEFORM by defining a material subject to steel phase transformations according to the scenarios listed in Table 6. To illustrate, a section at the pin center was considered and the history of temperature with corresponding phases as the pin moves away was monitored (Figure 33 , left). From Figures 33, it is clear that after exceeding 727°C pearlite starts to transform into austenite specifically at the stir zone. Then, after reaching the maximum temperature at about 2 seconds, the cooling stage starts. In the cooling stage, some of the austenite transforms to martensite and some transform back to pearlite. This formation of martensite was reported using a transmission electron microscope (TEM), shown in Figure 35, by [24] while using the same processing parameters. It is also worth mentioning that from Figures 35 one can notice that larger phase transformations take place at the advancing side as compared with the receding side. This may be expected given that larger deformations take place at that side compared with the receding side and, thus, resulting in higher temperatures (heating and cooling). Therefore, in order to increase welding speeds, some may add pre-heating sources to lower the cooling rate such as the laser assistant heating proposed by [24].

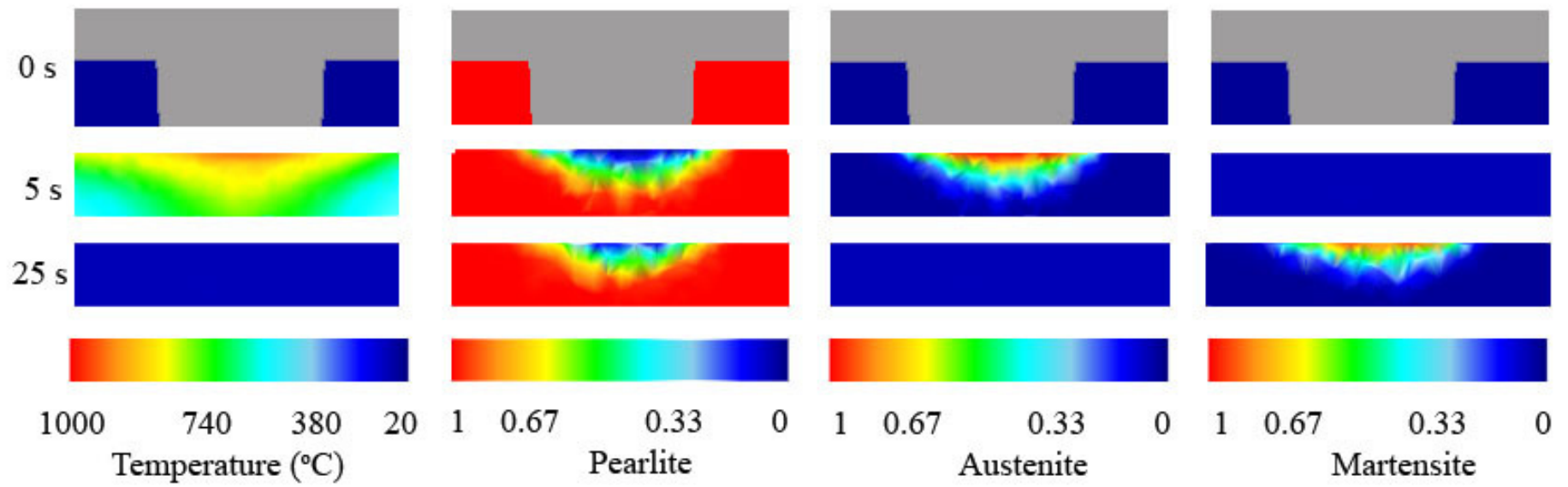


Figure 33:Phase transformation with time as the tool moves away for the normal friction stir welding (RPM=600; V=400 mm/min)

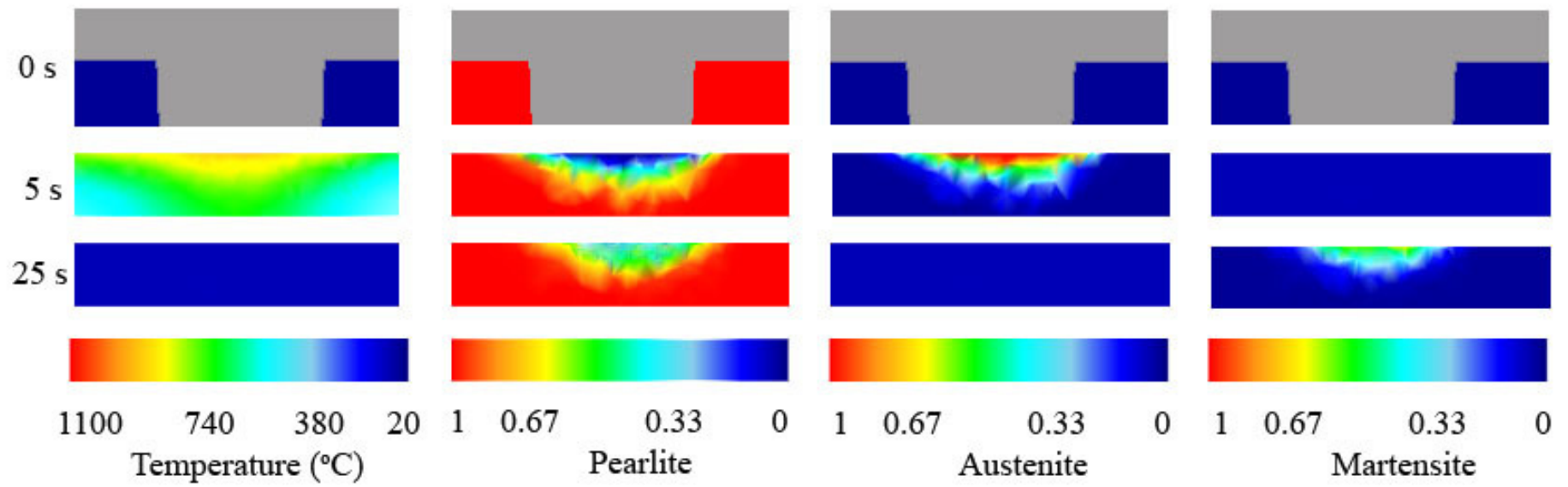


Figure 34: Phase transformation with time as tool moves away for laser assisted friction stir welding (RPM=600; V=400 mm/min)

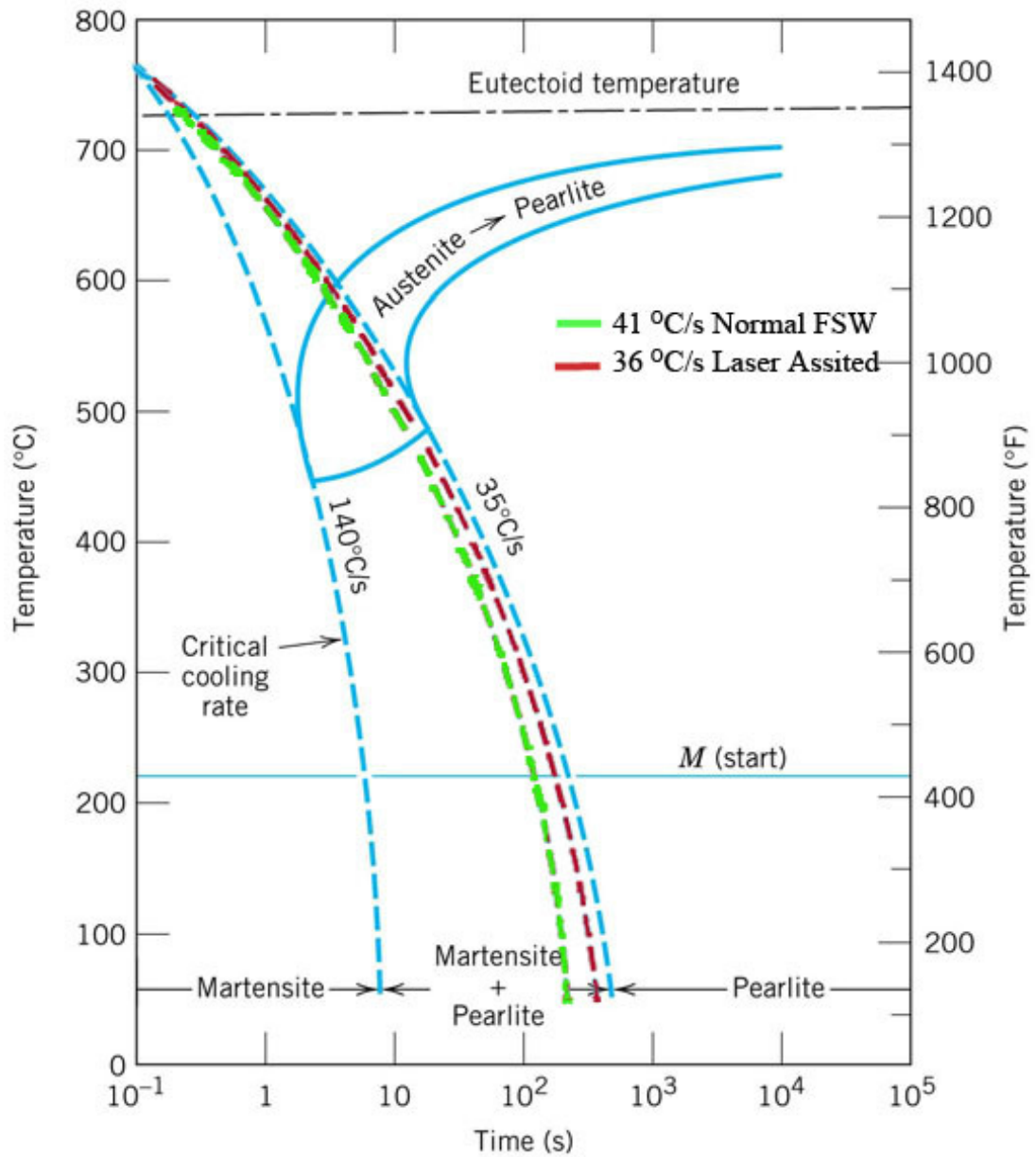


Figure 35: Continuous Cooling Transformation Diagram with FSW model cases superimposed

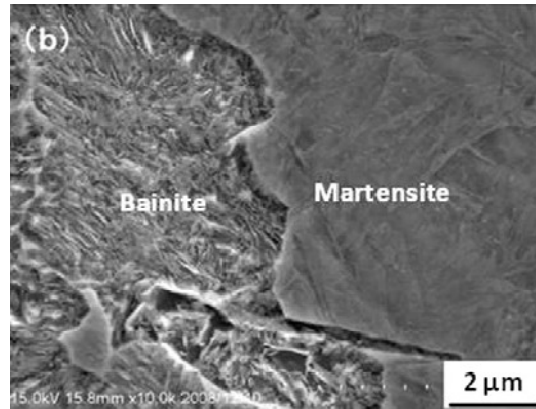


Figure 36: SEM image of the stir zone for transverse speed = 400 [24]

5. *Effect of In-process Laser Heating*

The application of laser increases the maximum temperature during FSW as shown in Figure 30 by about 100°C compared to normal FSW. This increase in temperature slowed the cooling rate which is believed to be behind martensite formation. The formation of brittle martensite in FSW joints is usually avoided. Therefore, in order to enhance the weld hardness and thus the weld sustainability some may add pre-heating sources to lower the cooling rate reducing martensite formation. Laser-assisted heating was found to be one method used to aid in heating of FSW steel joining [24]. To illustrate this fact more, the average cooling rate of both normal and laser assisted FSW were calculated and superimposed on a continuous cooling transformation diagram shown in Figure 35. It is shown from this figure how the laser assisted FSW aided in decreasing the cooling rate moving the curve toward the pearlite formation side. Moreover, with laser-assisted FSW, higher weld speeds can be achieved increasing the productivity and, thus, process and product sustainability. Contrasting Figure 33 with Figure 34, one can notice that less pearlite is transformed to martensite during in laser-assisted FSW. This is expected because the cooling rate decreases with the application of laser and also because more time is spent while cooling from higher peak temperatures.

K. Aluminum Magnesium Dissimilar Model

1. Model Validation

Validating this FEM model was accomplished by comparing its output with different experimental work published previously. Three validation criteria were set: 1) stirring action taking place, 2) aluminum magnesium interface, and 3) temperature histories at monitoring points.

a) Stirring Action

As mentioned above, particles in the work are continuously facing contact and separation conditions with the tool. To validate this complex process, the FEM results were compared to experimental results. In [52] steel shots were planted 1mm in the magnesium plate prior welding as in Figure 38 (from [52]). Then after welding, X-ray images were taken to detect the final position of the weld. On the other hand in the developed FEM, a particle was selected in the same position of the experiment and history tracking was applied. The tool rotational speed and linear feed were 1600 PRM and 35 mm/min respectively. If we compared the path traveled by the particle in FEM shown in Figure 37 and that of the steel shot shown in Figure 38, one can notice that they are in good agreement. The approximate angle α in FEM is slightly larger (5o) than angle β in experiment [52]. It is worth mentioning that such agreement was reached after tuning the separation criteria.

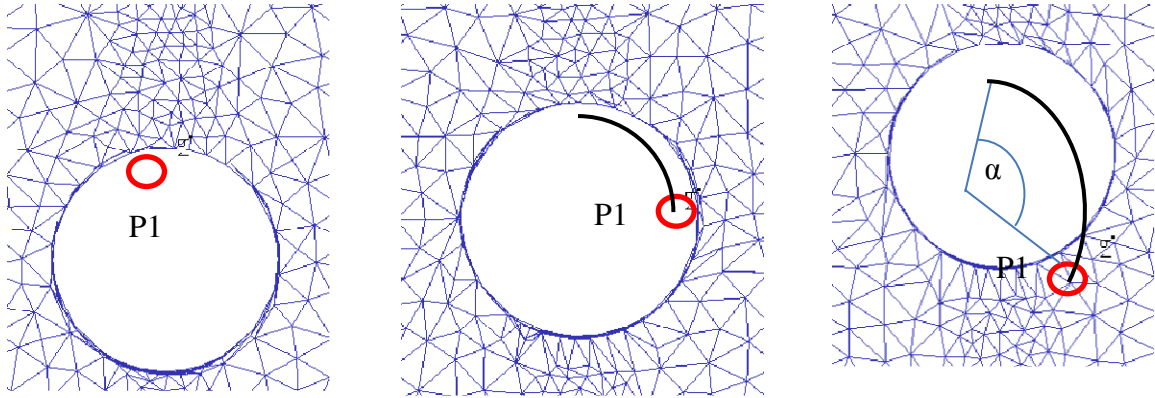


Figure 37: FEM point tracking snapshots from initial position (left) to final (right) for a particle placed in the magnesium plate.

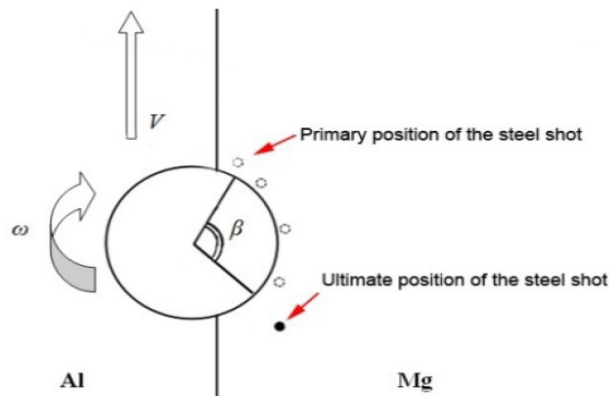


Figure 38: Steel shot initial and final positions [52]

b) Al/Mg Interface

To evaluate the developed FE model more, a section of the generated weld was taken and compared to experimental weld map done in [51]. The specimens were etched in a 5 ml acetic acid + 5 g picric acid + 10 ml water + 100 ml ethanol solution to reveal the Mg side of the weld. When comparing the experimental macrograph (a) [51] with FEM (b) weld section in Figure 39, one can notice that although two sections are not full agreement but a similar mixing pattern can be seen. More specifically, it is clear from the two sections how the magnesium (blue) invaded the aluminum side (red). Moreover, this invasion is more

severe at the upper part which is expected because in the as we move upwards the shoulder helps in the mixing process.

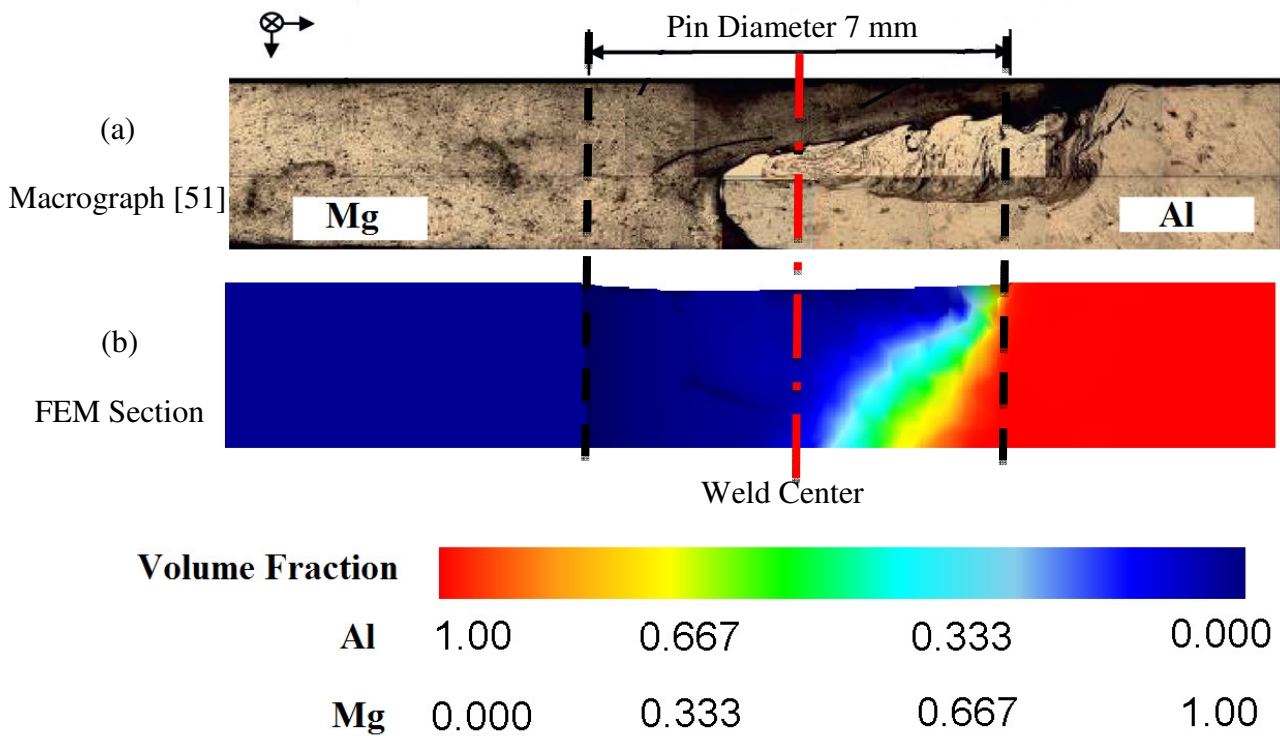


Figure 39: A comparison between the experimental macrograph (a) [51] and FEM weld section (b)

Furthermore, it is proved that during DFSW of aluminum and magnesium intermetallic compounds ($Al_3Mg_2, Al_{12}Mg_{17}$) are being formed. We can see from the Al/Mg phase diagram in Figure 40 the temperatures and compositions at which these compounds usually forms. Accordingly, in the FEM model the interface between aluminum and magnesium was implemented as a volumetric gradual change. Due to the lack of material properties and flow stress equations of the new intermetallic compound formed, the new phases for the intermetallic compounds were not defined. This issue was compensated with

the elements at the interphase having volume fractions from each of the two main materials where all the mechanical properties and flow equations follow these fractions. Moreover, this intermetallic layer formed is found to be a thin layer in the ranges of 100 micrometers as shown in the SEM (equipped with EDS) image in Figure 41. Therefore, to model this layer in FEM a very fine element size should be defined. In this model a minimum element size of 0.2mm was considered in order to minimize long simulation times.

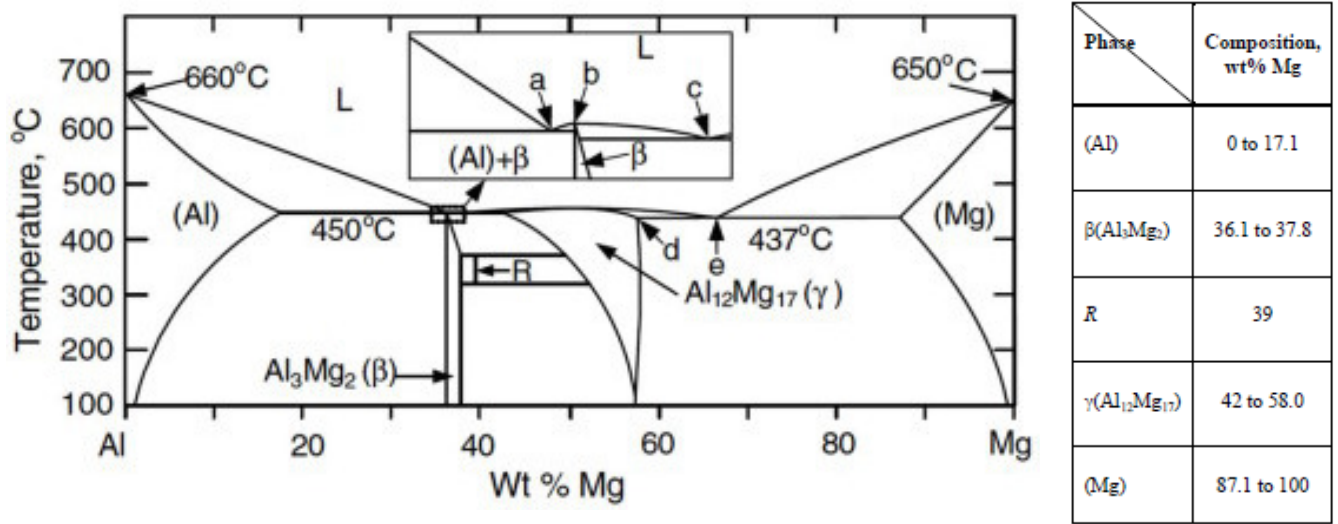


Figure 40: Al-Mg phase diagram (a) and crystallographic data (b) [84]

(a)

(b)

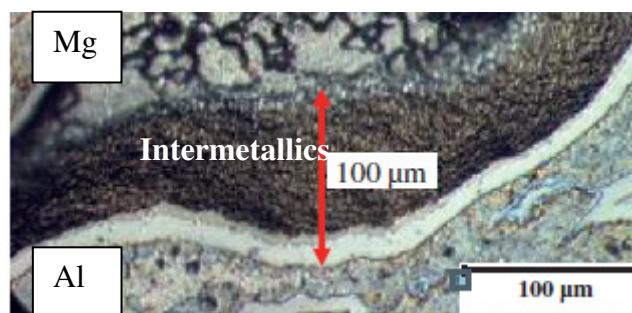


Figure 41: SEM image showing the microstructure of the Al/Mg interphase [51]

c) **Temperature Profiles**

In order to track the temperature history, two points of interest were selected. The first point was 6 mm from the weld line towards the magnesium retreating side; the second point was also 6 mm from the weld line but now towards the aluminum advancing side. The temperature was recorded as the tool passes near the points for a period of about 15 seconds. The tool rotational speed and linear feed were: 300 PRM and 50 mm/min respectively. On the other hand, an experiment [51] with all geometries matching our FEM was selected from literature as an experimental validation reference where temperature was monitored via thermocouples placed in the same aforementioned positions. Results comparing experimental to FEM simulations for the two points are plotted in Figures 42 and 43 (note that the FEM results are shown as line connecting the calculated data points because there are so many of them that it makes more sense to connect them). It is worth mentioning that the time shown on the x-axis is that of relative (welding) time. Both Figures showed matching peak temperatures between experimental and FEM with some minor differences. Moreover, if we compared the peak temperatures of both points we can realized that the peak temperature reached in aluminum (405 °C) is higher than the one reached in magnesium side (386 °C). This fact which can be reached numerical and experimentally was expected and several reasons are behind it. First, the material movement and thus plastic deformations are believed to be larger in the advancing side than that of the retreating side because the rotational movement matches the linear ones in advancing side. Second, the thermal conductivity of aluminum is higher than that of magnesium and thus aluminum is expected to absorb more heat generated from the tool- workpiece frictional forces.

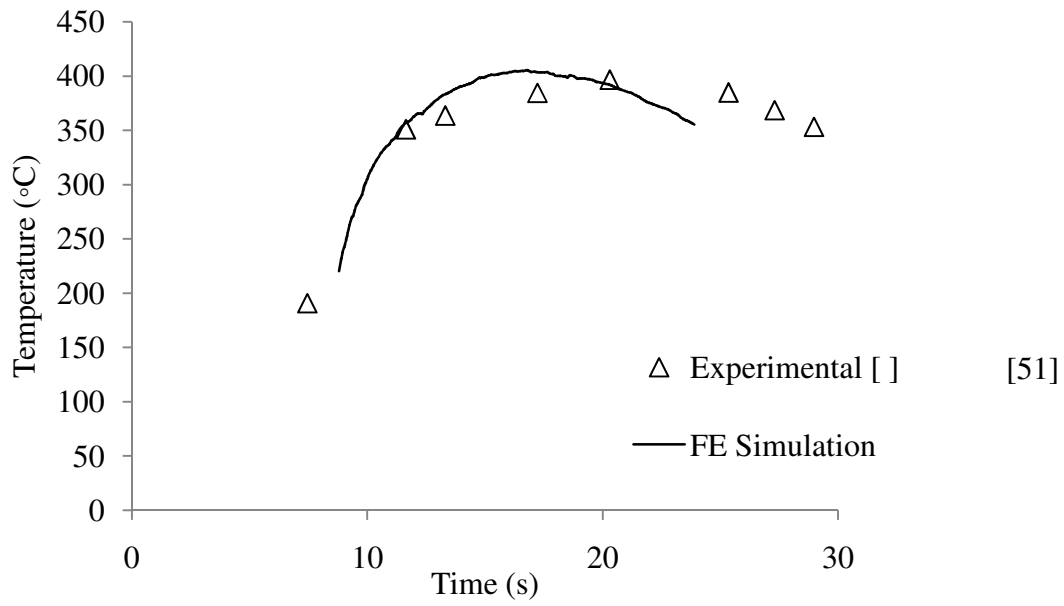


Figure 42: Temperature history for a point placed 6mm from the weld line in the aluminum advancing side

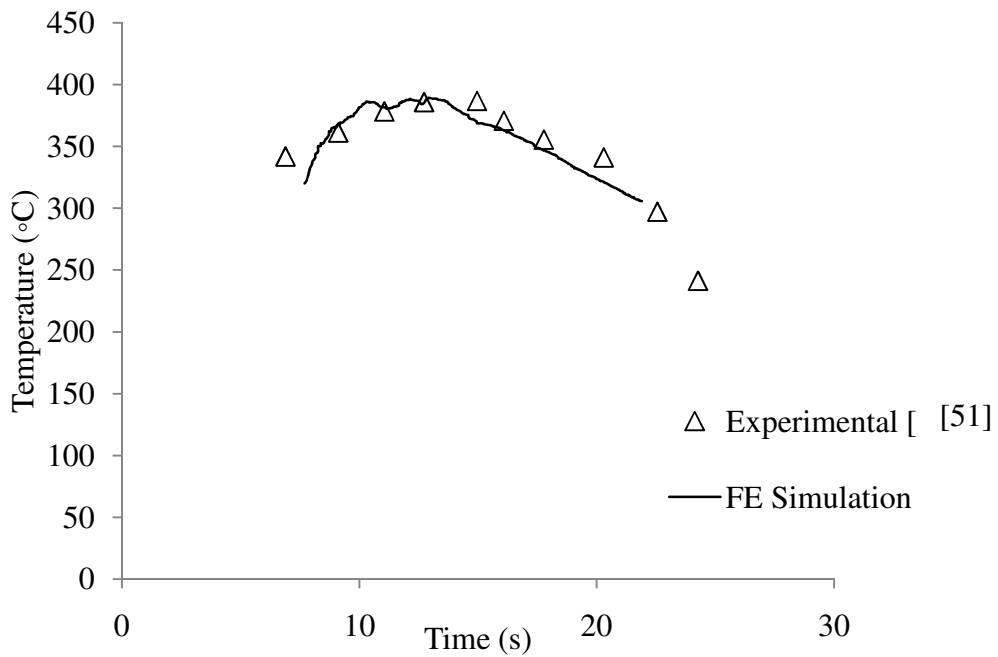


Figure 43: Temperature history for a point placed 6mm from the weld line in the magnesium retreating side

2. *Temperature Contours*

In any FSW, melting temperatures are usually avoided which are in this case 660 °C and 650 °C for aluminum and magnesium respectively. Therefore, temperatures which were validated before is an important variable to monitor during process. Furthermore, in DFSW liquefaction of intermetallic compounds formed may occur at temperatures lower than melting ones causing cracking and weld defects [51]. In Figure 44, the temperature history of the top surface of the workpiece is shown from the initial stage to the final stage. The maximum temperature reached is 530°C which is below the melting temperature of both materials. It is worth mentioning that this maximum temperature is higher than the previous validated one because that previous temperature was placed outside the weld zone (as in the experimental setup) and was also below the top surface.

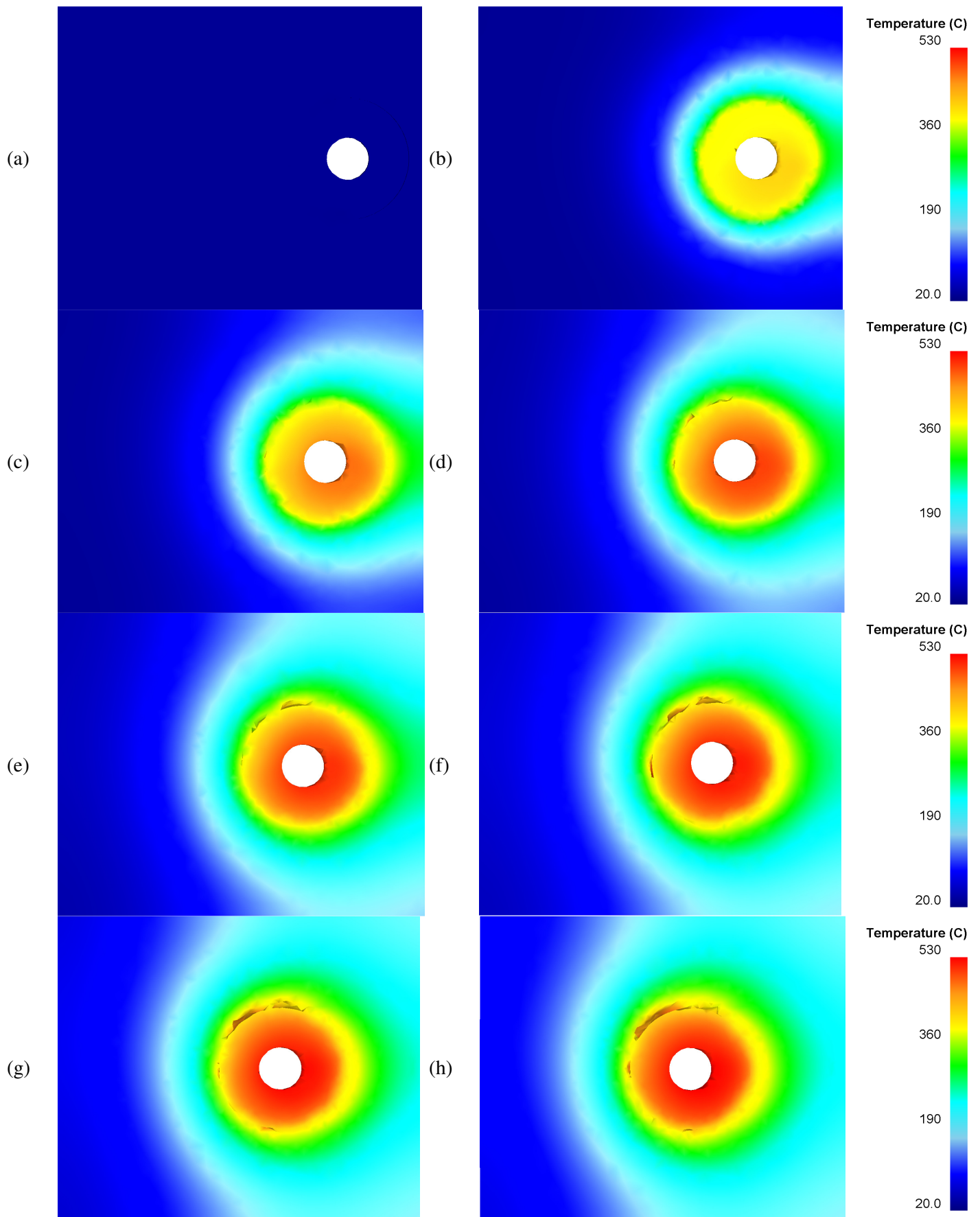


Figure 44: Workpiece Top surface temperature contours by time (a) to (h)

3. *Material flow*

To illustrate the material flow caused by the tool (pin and shoulder) snapshots of the material flow were considered. Sections were taken before, during and after the tool pass. Figure 45 shows the top view of the plates before and after mixing with volume fractions indicated. Additionally, sections were made before and after the pin passes are shown in Figure 46. The locations exact locations of the sections are shown in Figure 45.

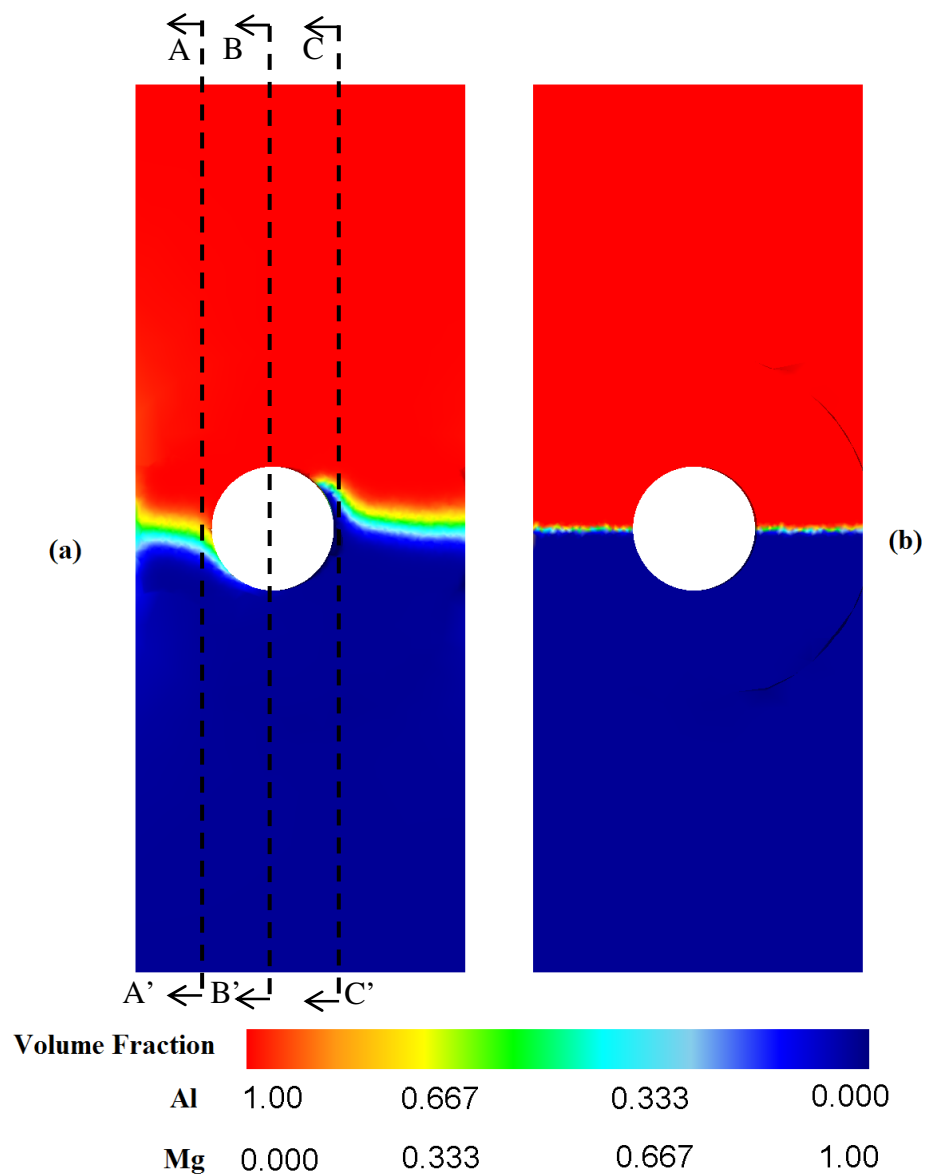


Figure 45: Top view Snapshots (b) before mixing (a) after mixing

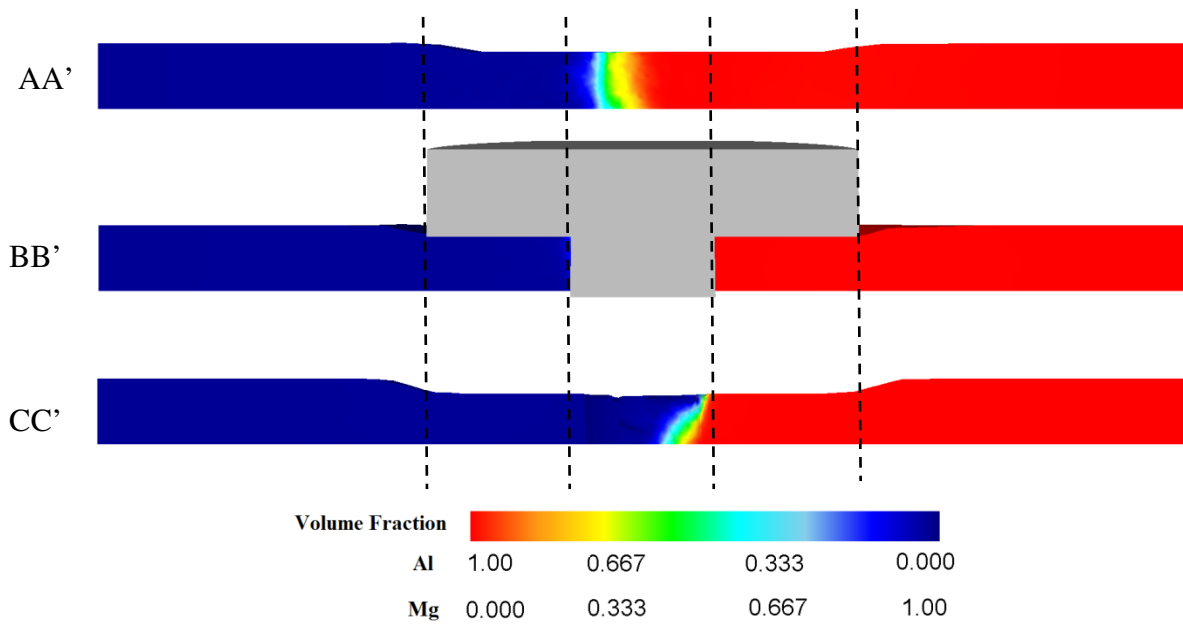


Figure 46: Sections before and after the pin during welding with locations shown in Figure 45

4. *Strain Profile*

It is well known that part of heat generated is due to plastic deformation. Therefore, it is necessary to check the strain profile of the weld section during FSW. DEFORM outputs total effective strain at the centroid of each element. From Figure 47 we can observe the effective strain at a section taken right behind the pin. Also from Figure 47 we can notice that the strain at the advancing side is also a bit larger than retreating side. This is due to the larger plastic deformation taking place at the harder metal placed at the advancing side (aluminum).

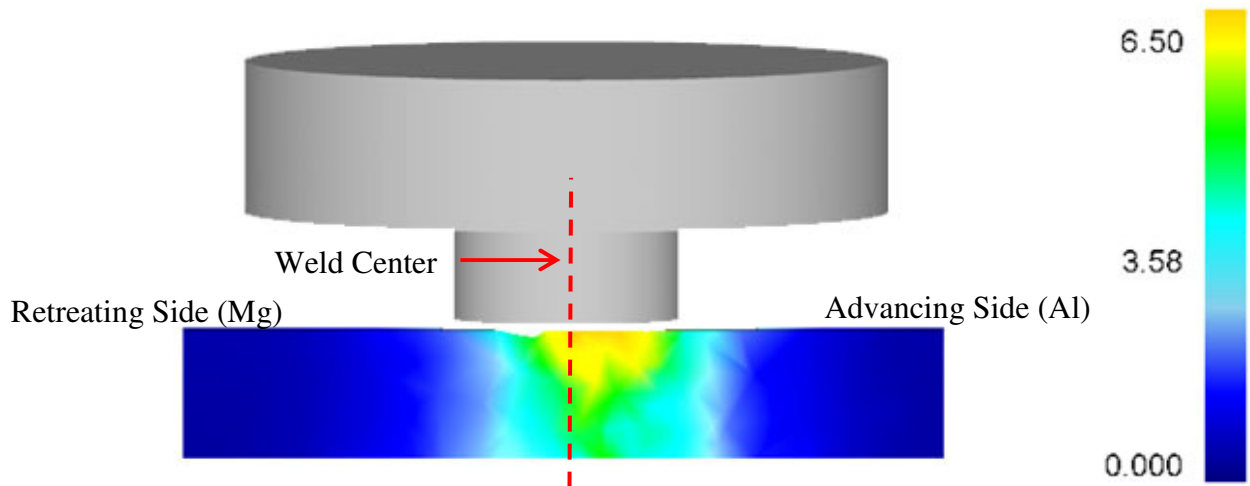


Figure 47: Effective strain (mm/mm) at the weld section right behind the pin of the tool

5. *Strain rate Profile*

The strain rate is another important state variable extracted from DEFORM. The strain rate is an indication for the rate of deformation taking place. The importance of this variable comes from its impact on the flow stresses and temperatures encountered.

Furthermore, it was mentioned before how the Zener-Hollomon parameter and thus resulting grain size are affected by strain rate. Therefore, it is necessary to monitor this variable in FSW. In Figure 48, the profile of strain rate in DFSW is shown. It can be observed that the strain rate is higher at the advancing side and it decreases as we move away from the pin. Moreover, the strain rate is higher at the top and decreases with depth. These conclusions are expected because the shoulder and the pin play an important role in material stirring action.

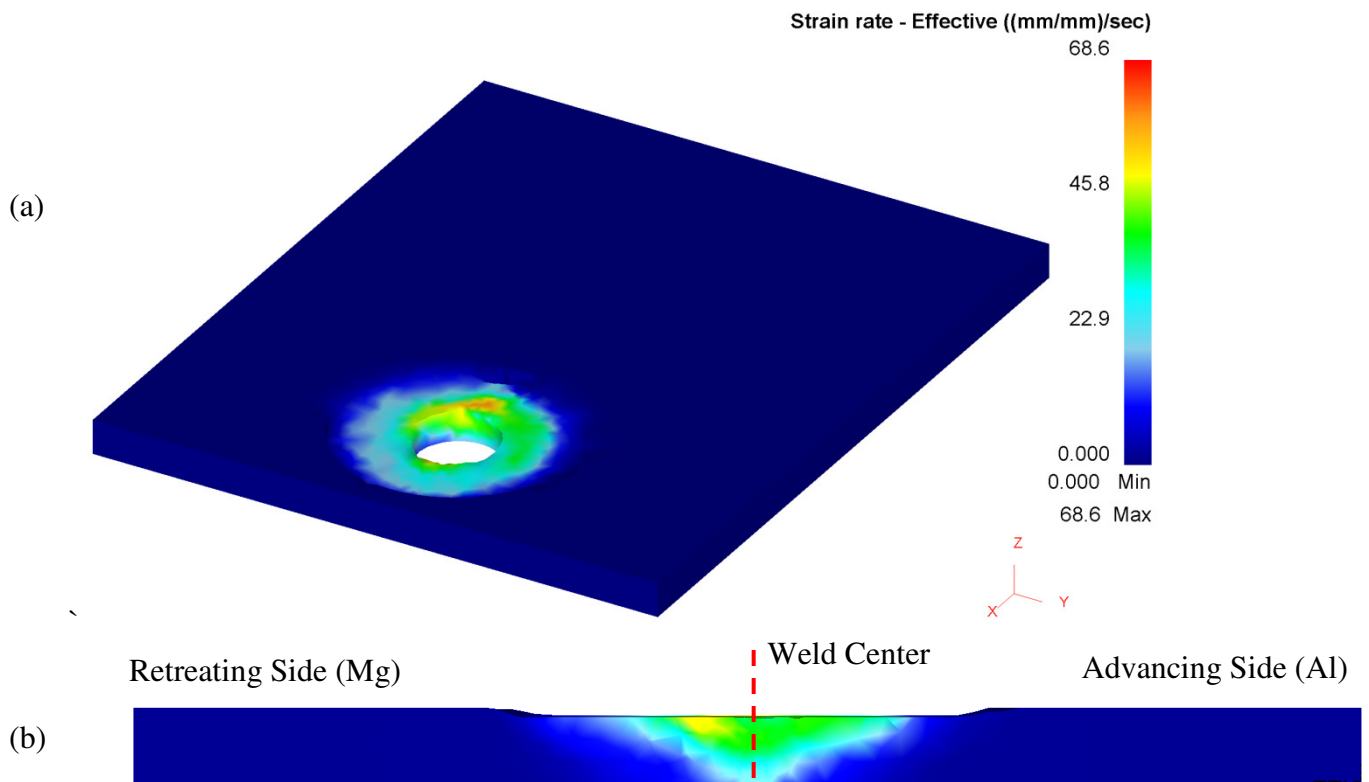


Figure 48: Effective strain rate during DFSW model (a) general profile (b) weld section

CHAPTER V

CONCLUSIONS

In this work four thermo-mechanical FE models were developed for friction stir welding:

- The first model successfully simulated the similar aluminum FSW process. The model was validated with previously reported experimental work by other researchers. The effect of two cooling techniques, back plate cooling and cryogenic CO₂ cooling, on grain size was investigated and the corresponding average grain size across the weld-line was predicted. Cryogenic cooling appears to have contributed to effective dynamic recrystallization and resulting in generating work material with sub micrometer grains along the weld line.
- The second model successfully simulated the similar magnesium FSW process. The model was validated with previously reported experimental work by other researchers .The model was used to investigate the different effects of the process parameters on the average grain size, the strain rate, and the maximum temperature at the observation point. It was noticed that at low tool rotational speeds the temperature didn't raise enough to perform successful processing and resulted in defects such as warm holes and voids in the processed material. Higher RPMs on the other hand resulted in melting at the tool-workpiece interface and thus deterioration of the surface can be expected with non-uniform grain size distribution. A reasonable tool rotational speed for processing AZ31b at a constant traverse speed of 90 mm/min should be in the range of 800-1100 RPM. Cooling the FSW process resulted in

decreasing the grain size of the welded material and thus enhancing the mechanical properties. Higher cooling rates corresponded to harder material due to the enhancements in the microstructure.

- The third model successfully simulated the similar steel FSW process. The simulation results of peak temperatures of the weld were validated against experimental work reported by other researchers. The effect of advancing speed on weld temperature was examined where peak temperatures were found to decrease with increasing traverse welding speed. With laser assistance, however, higher welding temperatures can now be reached faster at larger welding speed thus increasing the sustainability of the process. Furthermore, the resulting phase transformations, which have direct effect on the microstructure and, thus, the mechanical properties of the weld were successfully accounted in the model. It was found that with laser-assisted processing, smaller phase fraction of the brittle martensite phase is formed at the stir zone resulting in enhanced properties of the welded joint and, thus, enhancing weld sustainability. It is believed that such model can be used for optimization purposes leading to more sustainable processes and, more importantly, sustainable products.
- The fourth model was successfully simulated the dissimilar aluminum/magnesium FSW process. The model was validated with previously reported experimental work by other researchers. The model was successfully validated via criteria the following criteria: stirring action, Al/Mg interface and temperature profile. The model accurately predicted the non-symmetry of the weld including temperatures, strains and strain rates.

CHAPTER VI

Future Work

- As mentioned before, all the developed models were validated against literature. Now after preparing an FSW/FSP setup with all necessary sensors, instrumentation and data acquisition at AUB, it is possible to validate the models against local experimental results.
- After attempting Al/Mg DFSW joints can be used for material characterization, microstructural investigation, and chemical compositions. Then results can be compared to FEM model results.
- The dissimilar aluminum magnesium model can be enhanced by adding a phase transformations to the new intermetallic compound formed during DFSW.

CHAPTER VII

RELEVANT PUBLICATIONS

L. Refereed Papers

1. **Kheireddine**, A.H., Ammouri, A.H., Kridli, G.T., Hamade, R.F., “Fem Analysis of The Effects Of Cooling Techniques On The Microstructure Of Aluminum 7075 Friction Stir Welded Joints” Proceedings of the ASME 2012 International Mechanical Engineering Congress & Exposition IMECE 2012 November 9-15, 2012, Houston, Texas, USA. (Published)
2. Ammouri, A.H., **Kheireddine**, A.H., Hamade, R.F., “Model-Based Optimization of Process Parameters in the Friction Stir Processing of AZ31b with Active Cooling”. The 10th Global Conference on Sustainable Manufacturing. June 2012, Istanbul, Turkey. (Published)
3. **Kheireddine**, A.H., Ammouri, A.H., Lu, T., Jawahir, I.S., Hamade, R.F., “Experimental and FEM Analyses of the Effect of Liquid Nitrogen Cryogenic Cooling and other Processing parameters on the surface Hardness of Drilled Holes in AZ31b Magnesium” The 10th Global Conference on Sustainable Manufacturing. June 2012, Istanbul, Turkey. (Published)
4. Ammouri, A.H., **Kheireddine**, A.H., Kridli, G.T., Hamade, R.F., “A Numerical Model for Predicting the Zener-Hollomon Parameter in the Friction Stir Processing of AZ31B”. 8th international conference on processing & manufacturing of advanced materials. December 2013, Las Vegas, USA.(Accepted)
5. **Kheireddine**, A.H., Ammouri, A.H., Hamade, R.F., “FEM Analysis of Phase Transformations During Friction Stir Welding of AISI 1045 Carbon Steel”. 8th international conference on processing & manufacturing of advanced materials. December 2013, Las Vegas, USA. (Accepted)
6. **Kheireddine**, A.H., Ammouri, A.H., Lu, T., Jawahir, I.S., Hamade, R.F., “An FEM Analysis with Experimental Validation to Study the Hardness of In-Process Cryogenically Cooled Drilled Holes in Mg AZ31b”. 14th CIRP Conference on Modeling of Machining Operations, June 2013, Torino, Italy.(Accepted)
7. **Kheireddine**, A.A., Khalil, A.H., Ammouri, A.H., Kridli, G.T., Hamade, R.F., “An Experimentally Validated thermo-mechanical Finite Element Model for Friction Stir Welding in Carbon Steels” International Conference on Automation and Intelligent Manufacturing, ICAIM2013, April 2013, Johannesburg, South Africa. (Accepted)
8. Ammouri, A.H., **Kheireddine**, A.H., Kridli, G.T., Hamade, R.F., “Evaluating the Performance of Selected Constitutive Laws in the Modeling of Friction Stir Processing of AZ31b – Toward a More Sustainable Process”. The 11th Global

- Conference on Sustainable Manufacturing. September 2013, Berlin, Germany. (In Progress)
9. **Kheireddine**, A.H., Ammouri, A.H., Kridli, G.T., Hamade, R.F. “Finite Element Modeling of Laser Assisted Friction Stir Welding in Carbon Steels to Enhance Sustainability of Welded Joints”. The 11th Global Conference on Sustainable Manufacturing. September 2013, Berlin, Germany. (In Progress)
 10. **Kheireddine**, A.H., Ammouri, A.H., Kridli, G.T., Hamade, R.F., “Experimentally Validated Thermo-Mechanically Coupled FE Simulations Of Al/Mg Friction Stir Welded Joints” Proceedings of the ASME 2013 International Mechanical Engineering Congress & Exposition IMECE 2013 November 15-21, 2013, San Diego, CA, USA. (In Progress)
 11. Ammouri A.H., **Kheireddine**, A.H., Kridli, G.T., Hamade, R.F., “An Experimentally Verified Methodology for Controlling the Zener-Hollomon Parameter in the Friction Stir Processing of AZ31b” Proceedings of the ASME 2013 International Mechanical Engineering Congress & Exposition IMECE 2013 November 15-21, 2013, San Diego, CA, USA. (In Progress)

CHAPTER VIII

REFERENCES

- [1]. Mishra, R. S., and Ma, Z. Y. (2005). Friction Stir Welding and Processing. *Materials Science and Engineering Reports*, 50(1-2), 1-78.
- [2]. TWI website <http://www.twi.co.uk/technologies/welding-coating-and-material-processing/friction-stir-welding/>
- [3]. Andersson, C. G., and Andrews, R. E. (1999). Fabrication of containment canisters for nuclear waste by friction stir welding. *Proceedings of the First International Symposium on Friction Stir Welding*, Thousand Oaks, CA, USA.
- [4]. Andersson, C. G., Andrews, R. E., Dance, B. G. I.(1984). *Proceedings of the Second Symposium on Friction Stir Welding*, Gothenburg, Sweden. 5, 46.
- [5]. Hautala, T., and Tianien, T. (2003). *Proceedings of The Sixth International Conference On Trends In Welding Research*, Pine Mountain, GA, ASM International, 324.
- [6]. Lee, W. B., & Jung, S. B. (2004). The joint properties of copper by friction stir welding. *Materials Letters*, 58(6), 1041-1046.
- [7]. Park, H. S., Kimura, T., Murakami, T., Nagano, Y., Nakata, K., & Ushio, M. (2004). Microstructures and mechanical properties of friction stir welds of 60% Cu–40% Zn copper alloy. *Materials Science and Engineering: A*, 371(1), 160-169.
- [8]. Lee, W. B., Lee, C. Y., Chang, W. S., Yeon, Y. M., & Jung, S. B. (2005). Microstructural investigation of friction stir welded pure titanium. *Materials Letters*, 59(26), 3315-3318.
- [9]. Zhang, Y., Sato, Y. S., Kokawa, H., Park, S. H. C., & Hirano, S. (2008). Stir zone microstructure of commercial purity titanium friction stir welded using pcBN tool. *Materials Science and Engineering: A*, 488(1), 25-30.
- [10]. Juhas, M. C., Viswanathan, G. B., and Fraser, H. L.(2000). Microstructural Evolution in a Titanium Alloy Friction Stir Weld. *Proceedings of the Second Annual Symposium on Friction Stir Welding*, Gothenburg, Sweden.
- [11]. Juhas, M. C., Viswanathan, G. B., and Fraser, H. L. (2001). Microstructural Characterization of Aluminum Alloy Friction Stir Welds. *Proceedings of the Symposium on Friction Stir Welding*, New Orleans, LA, USA: TMS-ASM Annual Meeting,
- [12]. Lienert, T. J., Jata, K. V., Wheeler, R. (2001). *Proceedings of the Joining of Advanced and Specialty Materials III*, ASM International, Materials Park, OH, USA, 160.
- [13]. Ramirez, A. J., and Juhas, M. C. (2003). Microstructural Evolution in Ti-6Al-4V Friction Stir Welds. *Materials Science Forum*, 426-432(4), 2999-3004.
- [14]. Thomas, W. M., Threadgill, P. L., and Nicholas, E. D.(1999). Feasibility of Friction Stir Welding Steel. *Science and Technology of Welding and Joining*, 4(6), 365-372.
- [15]. Lienert, T. J., and Gould, J. E.(1999). *Proceedings of the First International Symposium on Friction Stir Welding*, Thousand Oaks, CA, USA,

- [16]. Lienert, T. J., Stellwag Jr., W. L., Grimmett, B. B.(2003). Friction Stir Welding Studies on Mild Steel. *Welding Journal*, 82(1), 1/s-9/s.
- [17]. Reynolds, A. P., Posada, M., DeLoach, J.(2001). FSW of Austenitic Stainless Steels. *Proceedings of the Third International Friction Stir Welding Symposium, Session 2, Kobe, Japan.*
- [18]. Park, S. H. C., Sato, Y. S., Kokawa, H. (2003). Rapid Formation of the Sigma Phase in 304 Stainless Steel during Friction Stir Welding. *Scripta Materialia*, 49(12), 1175-1180.
- [19]. Johnson, R., and Threadgill, P. L.(2003). *Proceedings of the Sixth International Conference on Trends in Welding Research, Vitek Pine Mountain, GA ASM International*, 88-92.
- [20]. Ozekcin, A., Jin, H. W., Koo, J. Y., Bangaru, N. V., Ayer, R., Vaughn, G., ... & Packer, S. (2004). A microstructural study of friction stir welded joints of carbon steels. *International Journal of Offshore and Polar Engineering*, 14(4).
- [21]. Cho, J. H., Boyce, D. E., & Dawson, P. R. (2005). Modeling strain hardening and texture evolution in friction stir welding of stainless steel. *Materials Science and Engineering: A*, 398(1), 146-163.
- [22]. Fujii, H., Cui, L., Tsuji, N., Maeda, M., Nakata, K., & Nogi, K. (2006). Friction stir welding of carbon steels. *Materials Science and Engineering: A*, 429(1), 50-57.
- [23]. Sato, Y. S., Nelson, T. W., Sterling, C. J., Steel, R. J., & Pettersson, C. O. (2005). Microstructure and mechanical properties of friction stir welded SAF 2507 super duplex stainless steel. *Materials Science and Engineering: A*, 397(1), 376-384.
- [24]. Sun, Y. F., Konishi, Y., Kamai, M., & Fujii, H. (2013). Microstructure and mechanical properties of S45C steel prepared by laser-assisted friction stir welding. *Materials & Design*, 47, 842-849.
- [25]. Liu, H. J., Fujii, H., Maeda, M., & Nogi, K. (2003). Tensile properties and fracture locations of friction-stir-welded joints of 2017-T351 aluminum alloy. *Journal of Materials Processing Technology*, 142(3), 692-696.
- [26]. Dawes, M. G., Karger, S. A., Dickerson, T. L., & Przyoatek, J. (2000). Strength and fracture toughness of friction stir welds in aluminum alloys. In *Proceedings of the Second International Symposium on Friction Stir Welding, Paper (No. S2-P1).*
- [27]. Biallas, G., Braun, R., Donne, C.D., Staniek, G., Kaysser, W.A. (1999). Mechanical properties and corrosion behavior of friction stir welded 2024-T3. *Proceedings of the First International Symposium on Friction Stir Welding, Paper No. S3-P3, CA, USA.*
- [28]. Benavides, S., Li, Y., Murr, L., Brown, D., & McClure, J. (1999). Low-temperature friction-stir welding of 2024 aluminum. *Scripta materialia*, 41(8).
- [29]. Hashimoto, T., Jyogan, S., Nakada, K., Kim, Y.G., Ushio M. (1999). FSW joints of high strength aluminum alloy. *Proceedings of the First International Symposium on Friction Stir Welding, Paper No. S9-P3, CA, USA.*
- [30]. Kinchen, D.G., Li, Z.X, Adams, G.P. (2003). Mechanical properties of friction stir welds in Al-Li 2195-T8. *Journal of Materials Processing Technology*, 142, 692-696
- [31]. Seidel, T. U., & Reynolds, A. P. (2001). Visualization of the material flow in AA2195 friction-stir welds using a marker insert technique. *Metallurgical and materials Transactions A*, 32(11), 2879-2884.

- [32]. Okamura, H. I. S. A. N. O. R. I., Aota, K., Sakamoto, M. A. S. A. H. I. K. O., Ezumi, M. A. S. A. K. U. N. I., & Ikeuchi, K. E. N. J. I. (2001). Behavior of oxide during friction stir welding of aluminum alloy and its influence on mechanical properties. *QJ Jpn. Weld. Soc*, 19, 446-456.
- [33]. Kumagai, M., Tanaka, S. (1999). Properties of aluminum wide panels by friction stir welding, in: *Proceedings of the First International Symposium on Friction Stir Welding*, Paper No. S3-P2, CA, USA.
- [34]. Sato, Y. S., Kokawa, H., Enomoto, M., & Jogan, S. (1999). Microstructural evolution of 6063 aluminum during friction-stir welding. *Metallurgical and Materials Transactions A*, 30(9), 2429-2437.
- [35]. J Hagström, J., & Sandström, R. (1997). Mechanical properties of welded joints in thin walled aluminium extrusions. *Science and Technology of Welding & Joining*, 2(5), 199-208.
- [36]. Mahoney, M. W., Rhodes, C. G., Flintoff, J. G., Bingel, W. H., & Spurling, R. A. (1998). Properties of friction-stir-welded 7075 T651 aluminum. *Metallurgical and materials transactions A*, 29(7), 1955-1964.
- [37]. Magnusson, L., Kallman, L. (2000). Mechanical properties of friction stir welds in thin sheet of aluminum 2024, 6013 and 7475. *Proceedings of the Second International Symposium on Friction Stir Welding*, Paper No. S2-P3, Gothenburg, Sweden.
- [38]. Lee, W. B., Kim, J., Yeon, Y. M.(2003). The Joint Characteristics of Friction Stir Welded AZ91D Magnesium Alloy. *Materials Transactions*, 44(5), 917-923.
- [39]. Esparza, J. A., Davis, W. C., Trillo, E. A. (2002). Friction-Stir Welding of Magnesium Alloy AZ31B. *Journal of Materials Science Letters*, 21(12), 917-920.
- [40]. Nagasawa, T., Otsuka, M., Yokota, T. (2000). Fracture and Mechanical Properties of Friction Stir Weld joints of Magnesium Alloy AZ31. *Magnesium Technology 2000*, 383-386.
- [41]. Nakata, K., Inoki, S., Nagano, Y.(2001). *Proceedings of the Third International Symposium on Friction Stir Welding*, Kobe, Japan, 27-28.
- [42]. Lee, W. B., Yeon, Y. M., and Jung, S. B.(2003). Joint properties of friction stir welded az31b - h24 magnesium alloy. *Materials Science and Technology*, 19(6), 785-790.
- [43]. Park, S. H. C., Sato, Y. S., and Kokawa, H.(2003). *Proceedings of the Sixth International Conference on Trends in Welding Research*, Pine Mountain, GA ASM International, 267.
- [44]. Kohn, G., Antonsson, S., and Munitz, A. (2000). Friction Stir Welding of Magnesium Alloys. *Automotive Alloys 1999*, 285-292.
- [45]. Johnson, R. (2003). Friction Stir Welding of Magnesium Alloys. *Materials Science Forum*. 419-422, 365-370.
- [46]. Esparza, J. A., Davis, W. C., and Murr, L. E.(2003). Microstructure-Property Studies in Friction-Stir Welded Thixomolded Magnesium Alloy AM60. *Journal of Materials Science*, 38(5), 941-952.
- [47]. Mahoney, M. W., Harrigan, W. H., and Wert, J. A. (1998). Friction stir welding SiC discontinuously reinforced aluminum. *Proceedings of the INALCO'98*, Cambridge, UK, 2, 231-236.
- [48]. Sato, Y. S., Park, S. H. C., Michiuchi, M., & Kokawa, H. (2004). Constitutional liquation during dissimilar friction stir welding of Al and Mg alloys. *Scripta Materialia*, 50(9), 1233-1236.

- [49]. Somasekharan, A. C., & Murr, L. E. (2004). Microstructures in friction-stir welded dissimilar magnesium alloys and magnesium alloys to 6061-T6 aluminum alloy. *Materials Characterization*, 52(1), 49-64.
- [50]. Yan, Y., Zhang, D. T., Qiu, C., & Zhang, W. (2010). Dissimilar friction stir welding between 5052 aluminum alloy and AZ31 magnesium alloy. *Transactions of Nonferrous Metals Society of China*, 20, s619-s623.
- [51]. Mofid, M. A., Abdollah-Zadeh, A., & Malek Ghaini, F. (2012). The effect of water cooling during dissimilar friction stir welding of Al alloy to Mg alloy. *Materials & Design*, 36, 161-167.
- [52]. Pourahmad, P., Abbasi, M., and Mehrabi, H. A., (2012). Bimetal friction stir welding of aluminum to magnesium. *Journal of Advanced Materials and Processing*, 1(1), 27.
- [53]. Simoncini, M., & Forcellese, A. (2012). Effect of the welding parameters and tool configuration on micro-and macro-mechanical properties of similar and dissimilar FSWed joints in AA5754 and AZ31 thin sheets. *Materials & Design*.
- [54]. Malarvizhi, S., & Balasubramanian, V. (2012). Influences of tool shoulder diameter to plate thickness ratio (D/T) on stir zone formation and tensile properties of friction stir welded dissimilar joints of AA6061Aluminium-AZ31B Magnesium alloys. *Materials & Design*.
- [55]. Colegrove, P. A., & Shercliff, H. R. (2005). 3-Dimensional CFD modelling of flow round a threaded friction stir welding tool profile. *Journal of Materials Processing Technology*, 169(2), 320-327.
- [56]. Schmidt, H., & Hattel, J. (2005). A local model for the thermomechanical conditions in friction stir welding. *Modelling and Simulation in Materials Science and Engineering*, 13(1), 77.
- [57]. Buffa, G., Hua, J., Shivpuri, R., & Fratini, L. (2006). A continuum based FEM model for friction stir welding—model development. *Materials Science and Engineering: A*, 419(1), 389-396.
- [58]. Butan, D., & Monaghan, J. (2009). Thermomechanical modelling friction stir welding aluminium 2024-T3. *International Journal of Computational Materials Science and Surface Engineering*, 2(1), 63-72.
- [59]. Buffa, G., Fratini, L., & Shivpuri, R. (2007). CDRX modelling in friction stir welding of AA7075-T6 aluminum alloy: Analytical approaches. *Journal of materials processing technology*, 191(1), 356-359.
- [60]. Richards, D. G., Prangnell, P. B., Withers, P. J., Williams, S. W., Nagy, T., & Morgan, S. (2008, May). Simulation of the effectiveness of dynamic cooling for controlling residual stresses in friction stir welds. In *7th international symposium friction stir welding*, TWI, Japan.
- [61]. Aval, H. J., Serajzadeh, S., & Kokabi, A. H. (2011). Thermo-mechanical and microstructural issues in dissimilar friction stir welding of AA5086–AA6061. *Journal of materials science*, 46(10), 3258-3268.
- [62]. Gupta, M. S. N., Balunaik, B., & Murti, K. G. K. (2012). Finite element modeling and thermo-mechanical analysis of friction stir welded al/cu bimetallic lap joints. *International Journal of Mechanical Engineering and Robotics Research*, 2(17), 165-173.
- [63]. Li, K., Aidun, D., and Marzocca, P. (2008). Modelling of the mixed weld zone of dissimilar metal joints by functionally graded materials” *STEEL GRIPS Journal of Steel and Related Materials*, 6(1), 58-68.

- [64]. Li, K., D. Aidun, and Marzocca P. (2009). 3-D thermo-mechanical analysis of friction stir welding of dissimilar metals using functionally graded material concept. Trends in welding Research, Proceedings of the 8th International Conference, Georgia, USA, 726-730.
- [65]. Li, K., Aidun, D., and Marzocca P. (2009). Time-varying functionally graded material thermal modeling of friction stir welding joint of dissimilar metals. Trends in welding Research, Proceedings of the 8th International Conference, 731-735.
- [66]. Oh, S. I., Wu, W. T., Tang, J. P., & Vedhanayagam, A. (1991). Capabilities and applications of FEM code DEFORM: the perspective of the developer. Journal of Materials Processing Technology, 27(1), 25-42.
- [67]. Aljoaba, S., Dillon Jr, O., Khraisheh, M., & Jawahir, I. S. (2012). Modeling the Effects of Coolant Application in Friction Stir Processing on Material Microstructure Using 3D CFD Analysis. Journal of materials engineering and performance, 21(7), 1141-1150.
- [68]. Cerri, E., Evangelista, E., Forcellese, A., & McQueen, H. J. (1995). Comparative hot workability of 7012 and 7075 alloys after different pretreatments. Materials Science and Engineering: A, 197(2), 181-198.
- [69]. EFUNDA online material library, "[Magnesium Alloy ASTM AZ31B-H24 material properties](#)". Access date 7/5/2012.
- [70]. Liu, G., Zhou, J., & Duszczkyk, J. (2008). Process optimization diagram based on FEM simulation for extrusion of AZ31 profile. Transactions of Nonferrous Metals Society of China, 18, s247-s251.
- [71]. McQueen H. J., Myshlaev M., Sauerborn M., Mwembela A. (2000). Flow Stress Microstructures and Modeling in Hot Extrusions of Magnesium Alloys," Magnesium Technology 2000, The Minerals, Metals and Materials Society, 355-362
- [72]. Schmidt, H., Hattel, J., & Wert, J. (2004). An analytical model for the heat generation in friction stir welding. Modelling and Simulation in Materials Science and Engineering, 12(1), 143.
- [73]. Nishioka, N., Chiang, L. F., Uesugi, T., Takigawa, Y., & Higashi, K. (2011). Dynamic Friction Properties and Microstructural Evolution in AZ 31 Magnesium Alloy at Elevated Temperature during Ring Compression Test. Materials Transactions, 52(8), 1575-1580.
- [74]. Liang, S. J., Liu, Z. Y., & Wang, E. D. (2009). Simulation of extrusion process of AZ31 magnesium alloy. Materials Science and Engineering: A, 499(1), 221-224.
- [75]. Ceretti, E., Fiorentino, A., & Giardini, C. (2008). Process parameters influence on friction coefficient in sheet forming operations. International Journal of Material Forming, 1(1), 1219-1222.
- [76]. Ammouri, A., Kheireddine, A., Hamade, R., (2012). Model-Based Optimization of Process Parameters in the Friction Stir Processing of AZ31b with Active Cooling. 10th Global Conference on Sustainable Manufacturing, Istanbul, Turkey.
- [77]. Chang, C. I., Lee, C. J., & Huang, J. C. (2004). Relationship between grain size and Zener–Holloman parameter during friction stir processing in AZ31 Mg alloys. Scripta Materialia, 51(6), 509-514.

- [78]. Callister, W. D., & Rethwisch, D. G. (2007). Materials science and engineering: an introduction. Nandan, R., Prabu, B., De, A., & Debroy, T. (2007). Improving reliability of heat transfer and materials flow calculations during friction stir welding of dissimilar aluminum alloys. WELDING JOURNAL-NEWYORK-, 86(10),313.\
- [79]. Nandan, R., Prabu, B., De, A., & Debroy, T. (2007). Improving reliability of heat transfer and materials flow calculations during friction stir welding of dissimilar aluminum alloys. WELDING JOURNAL-NEW YORK-, 86(10), 313
- [80]. Aerospace Specification Metal Incorporation
<http://asm.matweb.com/search/SpecificMaterial.asp?bassnum=MA5083H116>
 Access data 25/1/2013
- [81]. Kuykendall, K.(2011). An evaluation of Constitutive laws and their ability to predict flow stress over large variation in temperature, strain, strain rate characteristic of friction stir welding. PhD dissertation, Brigham Young University.
- [82]. Nourani, M., Milani, A., and Yannacopoulos, S. (2011). Taguchi optimization of process parameters in friction stir welding of 6061 aluminum alloy: a review and case study. Engineering, 3(2), 144-155.
- [83]. ASM handbook “ Binary alloy phase diagram” Vol .3 First edition 1992. 305-306